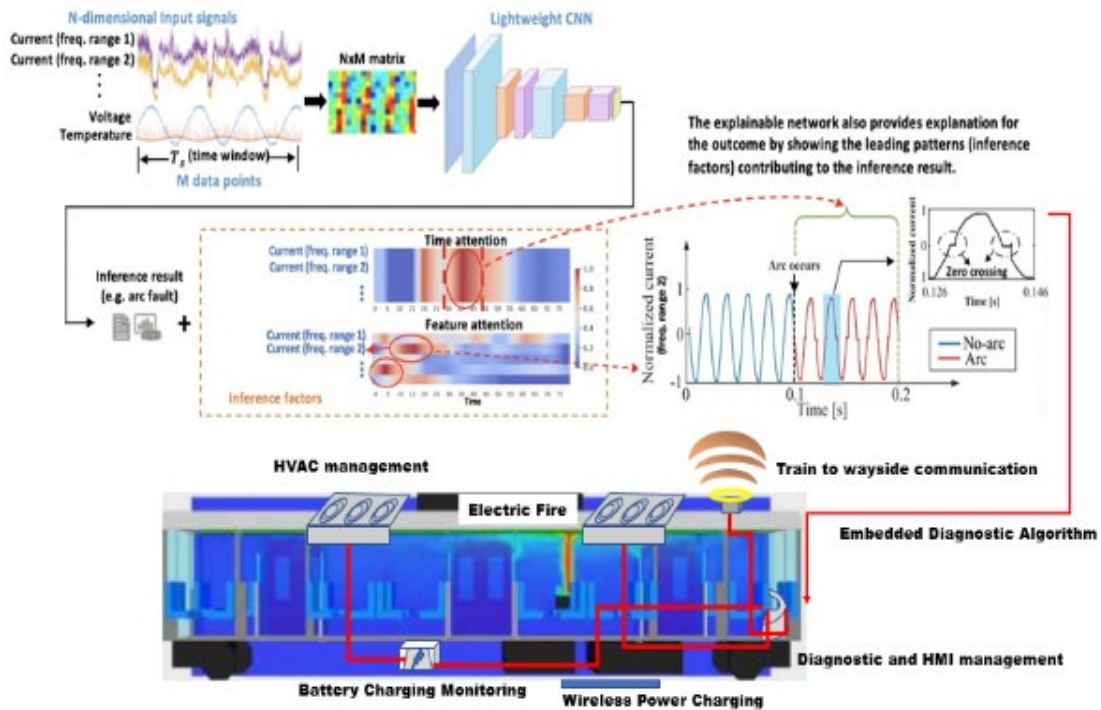




Intelligent Wireless Power Transfer (IWPT) for Safe Electric Power Charging of Rolling Stock



NOTICE

This document is disseminated under the sponsorship of the Department of Transportation in the interest of information exchange. The United States Government assumes no liability for its contents or use thereof. Any opinions, findings and conclusions, or recommendations expressed in this material do not necessarily reflect the views or policies of the United States Government, nor does mention of trade names, commercial products, or organizations imply endorsement by the United States Government. The United States Government assumes no liability for the content or use of the material contained in this document.

NOTICE

The United States Government does not endorse products or manufacturers. Trade or manufacturers' names appear herein solely because they are considered essential to the objective of this report.

REPORT DOCUMENTATION PAGE

Form Approved
OMB No. 0704-0188

The public reporting burden for this collection of information is estimated to average 1 hour per response, including the time for reviewing instructions, searching existing data sources, gathering and maintaining the data needed, and completing and reviewing the collection of information. Send comments regarding this burden estimate or any other aspect of this collection of information, including suggestions for reducing the burden, to Department of Defense, Washington Headquarters Services, Directorate for Information Operations and Reports (0704-0188), 1215 Jefferson Davis Highway, Suite 1204, Arlington, VA 22202-4302. Respondents should be aware that notwithstanding any other provision of law, no person shall be subject to any penalty for failing to comply with a collection of information if it does not display a currently valid OMB control number.

PLEASE DO NOT RETURN YOUR FORM TO THE ABOVE ADDRESS.

1. REPORT DATE (DD-MM-YYYY) 4/7/23		2. REPORT TYPE Technical Report		3. DATES COVERED (From - To) June 1, 2021–May 31, 2022	
4. TITLE AND SUBTITLE Intelligent Wireless Power Transfer (IWPT) for Safe Electric Power Charging of Rolling Stock				5a. CONTRACT NUMBER 693JJ621C000002	
				5b. GRANT NUMBER	
				5c. PROGRAM ELEMENT NUMBER BAA 2020 FRA-IRS-006	
				5d. PROJECT NUMBER	
6. AUTHOR(S) Tiefu Zhao, ORCid: 0000-0002-5548-8555 Nicole Braxtan, ORCid: 0000-0003-1315-0836 Shen-En Chen, ORCid: 0000-0002-5948-1238				5e. TASK NUMBER	
				5f. WORK UNIT NUMBER	
7. PERFORMING ORGANIZATION NAME(S) AND ADDRESS(ES) The University of North Carolina at Charlotte 9201 University City Boulevard Charlotte, NC 28223-0001				8. PERFORMING ORGANIZATION REPORT NUMBER	
9. SPONSORING/MONITORING AGENCY NAME(S) AND ADDRESS(ES) U.S. Department of Transportation Federal Railroad Administration Office of Railroad Policy and Development Office of Research, Development and Technology Washington, DC 20590				10. SPONSOR/MONITOR'S ACRONYM(S)	
				11. SPONSOR/MONITOR'S REPORT NUMBER(S) DOT/FRA/ORD-23/09	
12. DISTRIBUTION/AVAILABILITY STATEMENT This document is available to the public through the FRA website .					
13. SUPPLEMENTARY NOTES COR: Dr. Tarek Omar					
14. ABSTRACT To improve the safety of the electric power charging system for rolling stock, including both propulsion and ancillary use of stored electric power, this project proposes the use of Intelligent Wireless Power Transfer (IWPT) technology for power charging. The proposed IWPT technology removes humans from the process of locomotive battery charging, thus potentially reducing the chance of electrical shock to zero and improving the safety of the railroad environment from electrical fire. The IWPT system can assess rolling stock in motion and detect faulting and fire issues within the power circuits to significantly enhance rolling stock fire and electric safety.					
15. SUBJECT TERMS Rail safety, wireless power transfer, arc fault detection, battery fire safety, rolling stock, Intelligent Wireless Power Transfer, IWPT					
16. SECURITY CLASSIFICATION OF:			17. LIMITATION OF ABSTRACT	18. NUMBER OF PAGES	19a. NAME OF RESPONSIBLE PERSON
a. REPORT	b. ABSTRACT	c. THIS PAGE			19b. TELEPHONE NUMBER (Include area code)
				49	

METRIC/ENGLISH CONVERSION FACTORS

ENGLISH TO METRIC

LENGTH (APPROXIMATE)

1 inch (in)	=	2.5 centimeters (cm)
1 foot (ft)	=	30 centimeters (cm)
1 yard (yd)	=	0.9 meter (m)
1 mile (mi)	=	1.6 kilometers (km)

AREA (APPROXIMATE)

1 square inch (sq in, in ²)	=	6.5 square centimeters (cm ²)
1 square foot (sq ft, ft ²)	=	0.09 square meter (m ²)
1 square yard (sq yd, yd ²)	=	0.8 square meter (m ²)
1 square mile (sq mi, mi ²)	=	2.6 square kilometers (km ²)
1 acre = 0.4 hectare (he)	=	4,000 square meters (m ²)

MASS - WEIGHT (APPROXIMATE)

1 ounce (oz)	=	28 grams (gm)
1 pound (lb)	=	0.45 kilogram (kg)
1 short ton = 2,000 pounds (lb)	=	0.9 tonne (t)

VOLUME (APPROXIMATE)

1 teaspoon (tsp)	=	5 milliliters (ml)
1 tablespoon (tbsp)	=	15 milliliters (ml)
1 fluid ounce (fl oz)	=	30 milliliters (ml)
1 cup (c)	=	0.24 liter (l)
1 pint (pt)	=	0.47 liter (l)
1 quart (qt)	=	0.96 liter (l)
1 gallon (gal)	=	3.8 liters (l)
1 cubic foot (cu ft, ft ³)	=	0.03 cubic meter (m ³)
1 cubic yard (cu yd, yd ³)	=	0.76 cubic meter (m ³)

TEMPERATURE (EXACT)

$$[(x-32)(5/9)]^{\circ}\text{F} = y^{\circ}\text{C}$$

METRIC TO ENGLISH

LENGTH (APPROXIMATE)

1 millimeter (mm)	=	0.04 inch (in)
1 centimeter (cm)	=	0.4 inch (in)
1 meter (m)	=	3.3 feet (ft)
1 meter (m)	=	1.1 yards (yd)
1 kilometer (km)	=	0.6 mile (mi)

AREA (APPROXIMATE)

1 square centimeter (cm ²)	=	0.16 square inch (sq in, in ²)
1 square meter (m ²)	=	1.2 square yards (sq yd, yd ²)
1 square kilometer (km ²)	=	0.4 square mile (sq mi, mi ²)
10,000 square meters (m ²)	=	1 hectare (ha) = 2.5 acres

MASS - WEIGHT (APPROXIMATE)

1 gram (gm)	=	0.036 ounce (oz)
1 kilogram (kg)	=	2.2 pounds (lb)
1 tonne (t)	=	1,000 kilograms (kg) = 1.1 short tons

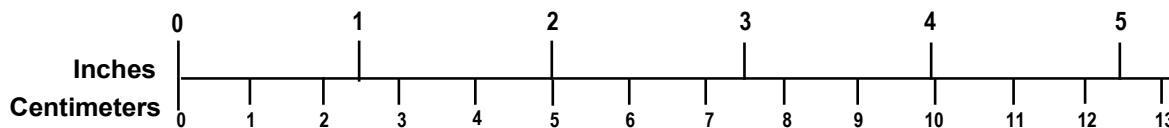
VOLUME (APPROXIMATE)

1 milliliter (ml)	=	0.03 fluid ounce (fl oz)
1 liter (l)	=	2.1 pints (pt)
1 liter (l)	=	1.06 quarts (qt)
1 liter (l)	=	0.26 gallon (gal)
1 cubic meter (m ³)	=	36 cubic feet (cu ft, ft ³)
1 cubic meter (m ³)	=	1.3 cubic yards (cu yd, yd ³)

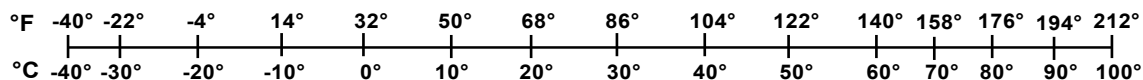
TEMPERATURE (EXACT)

$$[(9/5)y + 32]^{\circ}\text{C} = x^{\circ}\text{F}$$

QUICK INCH - CENTIMETER LENGTH CONVERSION



QUICK FAHRENHEIT - CELSIUS TEMPERATURE CONVERSION



For more exact and/or other conversion factors, see NIST Miscellaneous Publication 286, Units of Weights and Measures. Price \$2.50 SD Catalog No. C13 10286

Updated 6/17/98

Acknowledgements

The authors would like to thank Dr. Tarek Omar from the Federal Railroad Administration for guidance and technical discussions. The authors would also like to thank the following team members for their contributions to the project: University of North Carolina Charlotte graduate students Xiwen Xu, Karl Lin, Kamal Paul, Corbin Coe, Eric Huhn, and Mason Sun, and Mr. Dave Cook from Rail Propulsion Systems.

Contents

Executive Summary	1
1. Introduction.....	3
1.1 Background.....	3
1.2 Objectives	3
1.3 Overall Approach	3
1.4 Scope	4
1.5 Organization of the Report	4
2. IPT System.....	5
2.1 Design Considerations.....	5
2.2 Experimental Results.....	8
2.3 Packaging Design.....	10
3. AI-based Arc Fault Detection	12
3.1 System Architecture	13
3.2 Arc Generation and Data Collection Using Oscilloscope	15
4. Fire Safety Detection.....	17
4.1 Background of LIBs	17
4.2 Fire Safety Approach.....	20
4.3 Technical Results	21
4.4 Experimental Methods.....	22
4.5 Results and Observations.....	27
4.6 Sample Cylindrical Cell Battery Behavior	28
4.7 Comparison of Results	30
4.8 Summary.....	33
5. Conclusion	36
6. References.....	37

Illustrations

Figure 1. Conceptual diagram of wireless train charging application	5
Figure 2. Dimensional information of the proposed W-I shaped coupler.....	6
Figure 3. Magnetic flux density overlay of the W-I core.....	6
Figure 4. LCL-S compensated IPT system.....	8
Figure 5. IPT testbed setup	8
Figure 6. Experimental waveforms of the system operating at 5 kW.....	9
Figure 7. Power and efficiency variation of the IPT testbed.....	10
Figure 8. System efficiency measurement results for the IPT prototype.....	10
Figure 9. Belmont Trolley trailer.....	11
Figure 10. Demonstration diagram	11
Figure 11. Transmitter and receiver modules and package.....	11
Figure 12. Overall system architecture of the DC arc fault detection system.....	13
Figure 13. Arc generator with arcing electrodes.....	13
Figure 14. Designed signal conditioning board.....	14
Figure 15. Raspberry PI 4B.....	14
Figure 16. Arc generation and data collection setup with DC power supply and resistive loads .	15
Figure 17. Arc current and arc voltage recorded using oscilloscope.....	15
Figure 18. Normal current and arc current FFT	16
Figure 19. Typical LIB shapes [12].....	17
Figure 20. 18650 layering detail [14].....	18
Figure 21. Prismatic layering detail [15].....	18
Figure 22. ARC vs. SOC for batteries with different cathode materials [9].....	19
Figure 23. SOC impact on TR in 16 Ah automotive pouch cells [9].....	19
Figure 24. SOC relationships from tested cells [9].....	20
Figure 25. Current test system schematic.....	20
Figure 26. Candid test shot with PPE.....	21
Figure 27. Test box furnace detail	22
Figure 28. Adjusted hotplate mean heating curve	23
Figure 29. Hotplate detail with hot spot.....	24
Figure 30. POV of wireless system.....	25
Figure 31. Rijer prismatic charger	26

Figure 32. EASTSHINE cylinder charger.....	26
Figure 33. Pre-heating prism (LCO) placement	26
Figure 34. Standard 18650 cell placement	27
Figure 35. Endcap placement (May 3, 2022)	27
Figure 36. 18650 cell INR 100 percent 2,600 mAh (April 27, 2022, Test #3)	28
Figure 37. Post-test condition (April 27, 2022, Test #3).....	28
Figure 38. ~5 seconds after explosion (April 27, 2022, Test #3)	29
Figure 39. ~50 seconds after explosion (April 27, 2022, Test #3)	29
Figure 40. 1 Sec. pre-expl. (April 27, 2022, Test #3)	30
Figure 41. 1 Sec. post-expl. (April 27, 2022, Test #3).....	30
Figure 42. Prismatic LCO TR temp vs. time.....	31
Figure 43. 18650 IMR TR temp vs. time	31
Figure 44. 18650 INR TR temp vs. time.....	31

Tables

Table 1. FEA Results	7
Table 2. Circuit Parameters	9
Table 3. IMR SOC Comparison	32
Table 4. Intra-Chemistry Indicator Averages	33

Executive Summary

This project was funded by the Federal Railroad Administration (FRA) in reply to the 2020 Broad Agency Announcement (BAA). FRA contracted The University of North Carolina at Charlotte (UNCC) to conduct research to improve the safety of the electric power charging system for rolling stock, including both propulsion and ancillary use (i.e., air conditioning, lighting, and controls). This report summarizes the UNCC team's Phase 1 research findings and achievements from June 1, 2021, to May 31, 2022. The project team examined the use of Intelligent Wireless Power Transfer (IWPT) technology for power charging. The proposed IWPT system provides an automated charging process and completely removes humans from potentially hazardous environments and electric shock. Integrated with the intelligent fault protection and fire safety algorithms, the IWPT system also provides a safety inspection platform to assess rolling stock for safety risks, including damaged or deteriorating components, arcing fault, and fire risk. The proposed IWPT system introduces both static and dynamic (i.e., in motion) operation, which means the rolling stock in motion can be assessed without stopping. The system also reports the data and findings via a communication link for faulty component identification and train maintenance.

The research approach focused on the development and integration of three key technologies: wireless power transfer, artificial intelligence (AI)-based arc fault detection, and fire safety detection. In Year 1, the team completed the Inductive Power Transfer (IPT) prototype development and validated the 5 kW power transfer at Technology Readiness Level (TRL) 4. The prototype achieved an impressive efficiency of 92.5 percent DC to DC (DC-DC), which is the highest efficiency for rail applications reported in the literature. The team started the arc fault detection platform development and conducted initial data collection for future AI-based algorithm development. The team also developed a functioning wireless battery fire and explosion detection system (FEDS) and performed fire testing on several 18650 and small pouch batteries. All technical deliverables for Year 1 were completed on time. The key progress is summarized as:

1. IPT System Development. In Year 1, the team completed a W-I shaped IPT system prototype for railway system charging. The shape and size of the coupler was optimized to a W-I shape (a W-shaped transmitter (Tx) core and two I-shaped receiver (Rx) cores) to improve its power transfer capability. The LCL-S compensation topology can provide a constant track current that is irrelevant to the coupling coefficient and load conditions. Therefore, the communication between the transmitter and receiver is eliminated, simplifying the control system design. The testbed can be operated at a full rated power of 5 kW with a DC-DC efficiency of 92.5 percent, which is the highest IPT system efficiency reported for railway application. In Year 2, the team will complete system packaging design and integrate the proposed fault detection intelligence with the IWPT system.
2. AI-based Electrical Arc Fault Detection. DC arc faults in locomotive electrical systems are dangerous and may cause electrical fire hazards resulting in property damage as well as personnel injury. These arc faults have various causes including loose cable connections and trapped or faulty cables. As battery-powered rolling stocks are gaining increasing attention in recent years, the use of battery charging systems as well as the existence of other electrical power circuits may raise electrical safety issues like arc

faults. Therefore, arc faults need to be detected as soon as they occur, and the faulty parts need to be isolated from the functioning parts. The team proposed to develop an AI-based algorithm which will be able to detect arc fault in the power circuitry at a very high accuracy and at a very early stage of occurrence. The AI-based algorithm should be able to detect an arc fault with more than 99 percent accuracy. In Year 1 of this project, researchers completed an experimental setup for arc generation as well as arc fault data collection. The team also performed Fast Fourier Transform (FFT) analysis of the arc fault data to observe the differences between the normal and arc current. In Year 2, the team plans to complete the arc fault detection prototype and develop a real-time, high-accuracy, AI-based detection algorithm to improve the electric safety of rolling stocks.

3. Fire Safety Detection. Lithium-ion battery (LIB) fire and explosion hazards are a major industry concern for producers and consumers. A better understanding of how LIBs behave leading up to and during explosion/fire events may lead to more effective detection, prevention, and suppression of these events. A full test matrix was analyzed and divided into subcategories of important findings. Initial findings showed that the state of charge (SOC) has an inverse relationship to the time of onset of thermal runaway (TR), but a direct relation to the intensity of energy release in TR. Looking ahead, the research team plans to integrate gas and voltage sensors into the experimental setup, test mid-sized (i.e., laptop-sized) batteries, and develop prediction tools for battery fire diagnosis. The additional LIB tests and a more evenly spread number of specific SOC increments will lead to a higher statistical significance for the test results and greater confidence in conclusions made from the test results.

1. Introduction

This project was funded by the Federal Railroad Administration (FRA), in reply to the 2020 Broad Agency Announcement (BAA). FRA contracted The University of North Carolina at Charlotte (UNCC) to conduct research to improve the safety of the electric power charging system for rolling stock, including both propulsion and ancillary use (i.e., air conditioning, lighting, and controls). The project team examined the use of Intelligent Wireless Power Transfer (IWPT) technology for power charging. The proposed IWPT system provides an automated charging process and completely removes humans from potentially hazardous environments and electric shock. This report summarizes the UNCC team's Phase 1 research findings and achievements from June 1, 2021, to May 31, 2022.

1.1 Background

This project studied an IWPT system for safe electric power charging of rolling stock. Currently, when electric locomotives are not in operation, they are plugged into electrical ground power (typically 480 V/400 A three-phase) to keep their batteries charged. The plug-in procedure requires parking the vehicles at specific locations and physically attaching a heavy charging cable to the locomotive. The physical attachment of the cable can potentially cause back pain, tripping personnel working on the tracks, and other labor safety-related risks. This process is also tedious and requires time to secure the adaptor to the train battery, a procedure which, when not done right, can cause arc faulting and electric fire. Furthermore, the wear and tear on the physical cable adaptors can be a nuisance cost in the long run and a potential source of fire and/or electrical shock. This is especially critical for lithium-ion batteries (LIBs).

Using state-of-the-art wireless power charging, locomotives can be equipped with electrical receivers and simply park over an electrical charging mat embedded under the rail, thus completely removing the physical labor involved in the power connection and reducing human exposure to arc fault or fire ignition mechanisms from electric wire connections. Aside from increased worker safety, implementation of IWPT charging stations would also afford time savings for workers and would be a technological step forward for the rail industry.

1.2 Objectives

The project team studied how an IWPT system can be used for safe electric power charging of rolling stock. The team examined how IWPT technology can completely remove humans from the process of locomotive battery charging, thus reducing the chance of electrical shock to zero and improving the safety of the railroad environment from electrical fire. The team studied the potential for IWPT systems to assess rolling stock in motion and detect faulting and fire issues within the power circuits to significantly enhance rolling stock fire and electric safety.

1.3 Overall Approach

The team's approach focused on the development and integration of three key technologies: a wireless power transfer system, artificial intelligence (AI)-based arc fault detection, and fire safety detection. The team performed demonstration tests of the IWPT power charging and fire detection capabilities, including verification and validation of the fire detection and power charging processes. Toward this goal, a 5 kW IWPT prototype was assembled, including AI-

based arc fault and fire safety detection functions, capable of both laboratory and field (rolling stock) demonstrations.

1.4 Scope

The scope of work for the project included the demonstration of the IWPT power charging and fire detection capabilities. The team performed demonstration tests including verification and validation of the fire detection and power charging processes.

1.5 Organization of the Report

[Section 1](#) outlines the research project. [Section 2](#) introduces the design, implementation, and experimental testing of the Inductive Power Transfer (IPT) system. [Section 3](#) discusses the initial setup and data collection of the AI-based arc fault detection system. [Section 4](#) describes the technical approach and experimental results regarding fire safety detection. Finally, [Section 5](#) presents the team's research conclusions.

2. IPT System

This section introduces the IPT system design for charging locomotives. Based on the characteristics and constraints of the rail system [1-5], a W-I shaped coupler was proposed, which is shown to achieve a higher coupling coefficient and uses a lower volume of the core material. Researchers conducted finite element analysis (FEA) using ANSYS Maxwell to optimize the W-I core design. The volume comparison of the core material was conducted in terms of cost evaluation. A prototype of the W-I coupler-based IPT system was developed to validate the design. The prototype was tested at 5 kW with a system efficiency of 92.5 percent.

2.1 Design Considerations

Figure 1 shows a conceptual IPT system for wirelessly charging a train. The IPT system for rail application contains a transmitter infrastructure embedded between the tracks and an on-board receiver system located on the underbelly of the locomotive. Direct current (DC) power is converted to a high frequency, alternating current (AC) power and injected into the transmitter coil by an inverter. The power is transferred wirelessly by coupled coils with an airgap. During power transfer, energy is transduced from electrical energy to magnetic energy by Ampere's law¹ in the transmitter and then transduced back to electrical energy based on Faraday's law² in the receiver. The compensation circuits on the transmitter and receiver are resonant with the transmitter and receiver coils, respectively, with objectives to reduce volt-ampere (VA) rating as well as maximize the power transfer capability. The high frequency-induced voltage on the receiver side is converted to DC voltage by a rectifier. A DC to DC (DC-DC) converter might be used to control the power flow from the receiver to the batteries and loads. Therefore, the IPT design must consider both magnetic design (coupler) and electrical design (compensation circuits and converters).

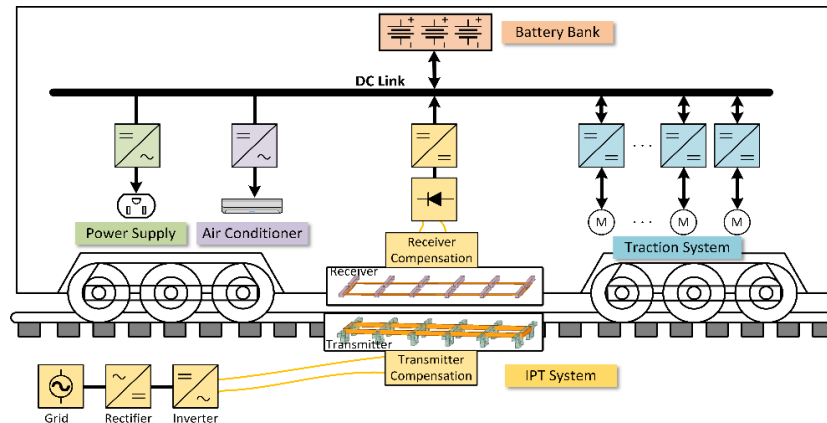


Figure 1. Conceptual diagram of wireless train charging application

¹ Ampere's law: The magnetic field created by an electric current is proportional to the size of that electric current with a constant of proportionality equal to the permeability of free space.

² Faraday's law: The electromotive force around a closed path is equal to the negative of the time rate of change of the magnetic flux enclosed by the path.

The power transfer capability for the coupler design is directly affected by the coupling coefficient, k . The shape and size of the coupler should be designed to achieve a higher k value in order to improve the transferred power level. The dimensions of the coupler are constrained by the track gauge and the locomotive chassis size. Since the tracks are made of iron, the edge of the coupler should not be too close to the tracks as this could lead to magnetic losses by generating stranded eddy currents within the tracks.

Based on the constraints and requirements discussed above for wireless locomotive charging, a W-I shape coupler (Figure 2) was proposed for the IPT system for rail application. The coupler consists of a W-shaped transmitter (Tx) core and two I-shaped receivers (Rx). The core material is Ferroxcube 3C90 (relative permeability of 2,300). The airgap of the coupler is designed to be 5 in (12.7 cm). To achieve the highest coupling coefficient k and to increase the output power transfer capability, the shape and size of the coupler and the position of the coils were optimized via ANSYS Maxwell. The coupler was designed to be a modular, discrete, distributed system along the tracks, and optimization was conducted on the design parameters to achieve a higher k value. The FEA results of the optimized W-I coupler are shown in Figure 3 and Table 1.

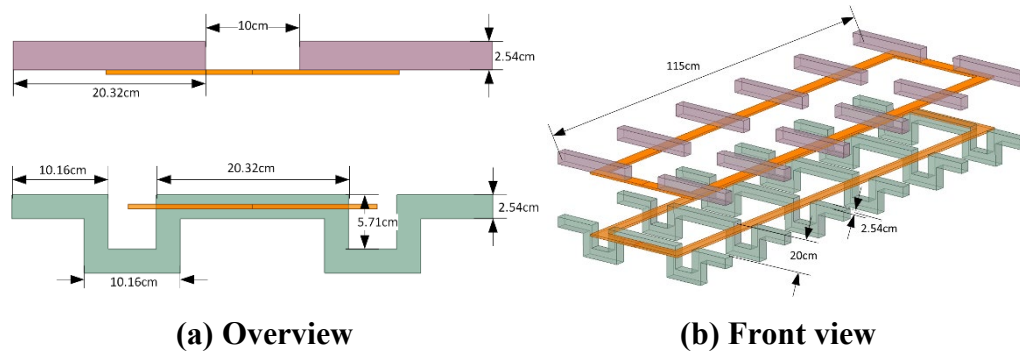


Figure 2. Dimensional information of the proposed W-I shaped coupler

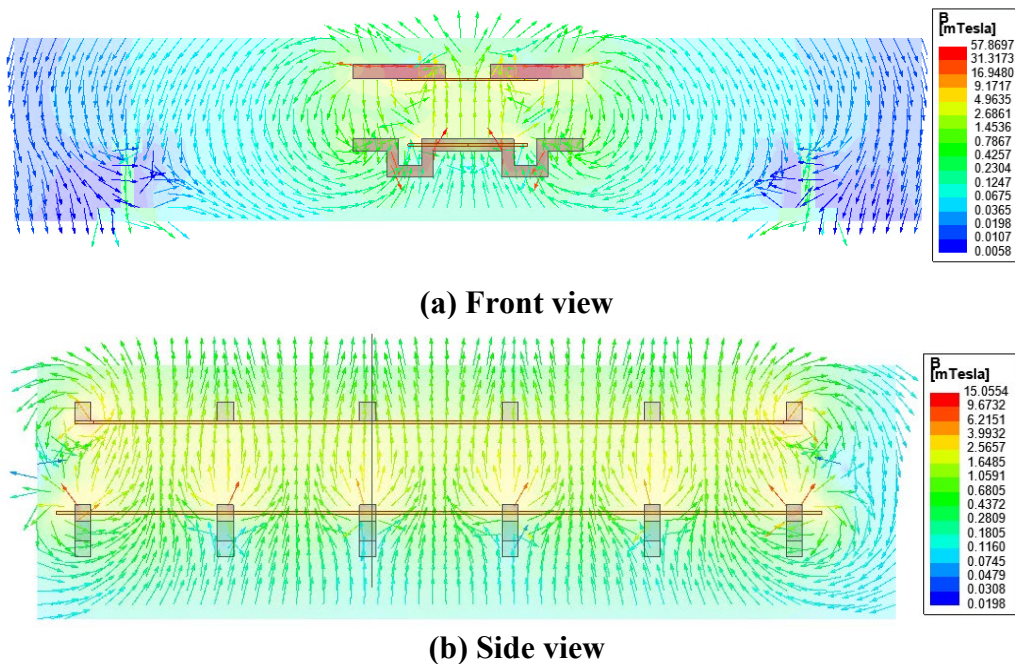


Figure 3. Magnetic flux density overlay of the W-I core

Table 1. FEA Results

Parameter	Symbol	Value
Tx self-inductance	L_p	74.4 μ H
Rx self-inductance	L_s	88.4 μ H
Mutual Inductance	M	18.6 μ H
Coupling coefficient	k	0.229
Airgap	D_{Air}	5 in

Since the standard length of a locomotive is 20 m, the coupler length has considerable design flexibility. However, a longer coupler would result in higher magnetic material cost, as well as increase the difficulty of the installation of a single-piece coupler system. The minimum required distance from the bottom of the locomotive to the top of the tracks defines the airgap between the coupler for the locomotives, which leads to the IPT system becoming a loosely coupled system. Therefore, achieving a higher coupling coefficient k becomes one of the main objectives to improve the power transfer capability of a loosely coupled IPT system. Toward this goal, core material with a higher permeability is required to achieve a higher k value.

As a wireless charging system for railway applications, the coupler design should be capable of both stationary and dynamic charging. Current proposed couplers for train applications, such as I-type coupler designs, have relatively high k values, but require precise positions on which the power transfer capability is fully realized. Since it is difficult to park the locomotive at a precise spot when stationary, it is inevitable for a locomotive to be parked at a null position with almost zero power transfer capability. The null position of I-type designs significantly reduces the reliability of the IPT system during stationary charging.

Compared to a tightly coupled system, loosely coupled IPT systems require compensation circuits on both transmitter and receiver sides, which reduce the VA rating on the source and load sides and maximizes the power transfer capability. As previously stated, there is some degree of difficulty parking a locomotive at a precise charging position, and as a result, the coupling coefficient may vary each time the locomotive is parked on the top of the transmitter. Therefore, a constant track current irrelative to the coupling coefficient is desired to provide a constant magnetomotive force to the receiver and ensure the stability of the power transfer process. For this reason, an LCL-S compensation topology was selected for the IPT system for railway application (Figure 4). By analyzing the equivalent circuit via Kirchhoff's circuit law³, the track current only depends on the input voltage V_{in} , switching frequency ω , and resonant capacitor C_R . The track current can be kept constant while the coupling coefficient k and the load R_{ac} vary. The LCL-S compensation circuit also provides a load-independent output voltage and

³ Kirchhoff's circuit laws are two equalities that deal with the current and potential difference (commonly known as voltage) in the lumped element model of electrical circuits. Kirchhoff's current law: the algebraic sum of currents in a network of conductors meeting at a point is zero. Kirchhoff's voltage law: the directed sum of the potential differences (voltages) around any closed loop is zero.

can achieve soft switching while the system operates at the designed operating frequency. The design constraints of the LCL-S compensation circuits are $\omega L_R = 1/\omega C_R$, $L_R = L_P$, and $\omega L_S = 1/\omega C_S$, respectively.

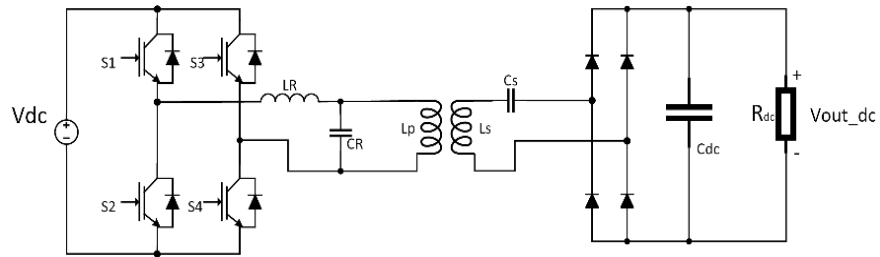


Figure 4. LCL-S compensated IPT system

2.2 Experimental Results

The output power of the IPT testbed was successfully pushed up to 5 kW with the optimized design. [Figure 5](#) shows the setup of the testbed. The transmitter system is located at the bottom of the cart and contains a SiC MOSFET high-frequency inverter and an LCL compensation network. The power transfers wirelessly from the transmitter coil to the receiver coil via the W-I shaped coupler. The receiver system is located at the top of the cart, consisting of a SiC Schottky diode rectifier and a high-power resonant capacitor bank in series. The electronic load and power resistors provided a load of 8.5 Ohm. The measured parameters of the IPT prototype are shown in [Table 2](#).

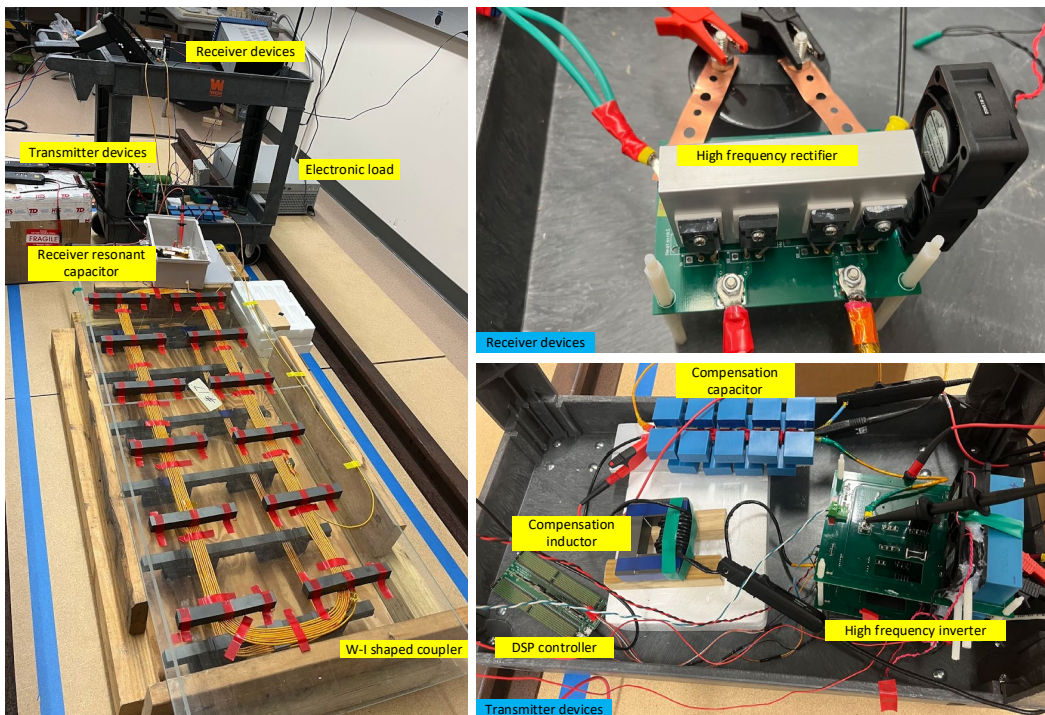
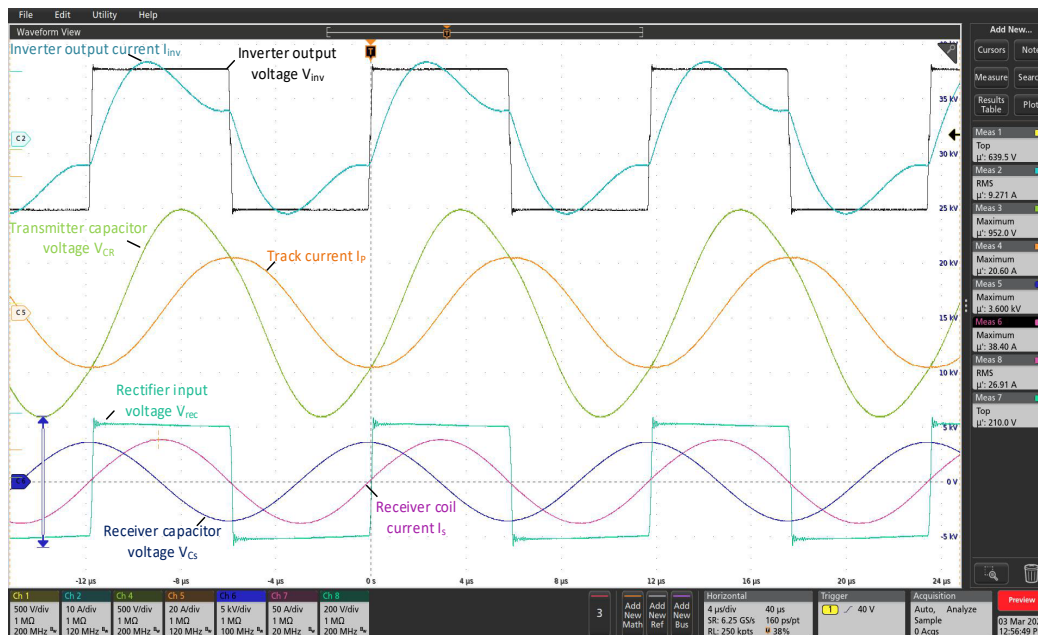


Figure 5. IPT testbed setup

Table 2. Circuit Parameters

Parameter	Symbol	Value
Frequency	f	85 kHz
Tx self-inductance	L_p	74.6 μ H
Rx self-inductance	L_s	88.7 μ H
Coupling coefficient	k	0.215
Tx resonant inductor	L_R	74.6 μ H
Tx capacitor	C_R	47.0 nF
Rx capacitor	C_s	39.5 nF

Figure 6 shows the experimental waveforms when the system operated at 5 kW. The inverter operated at a zero voltage switching (ZVS) condition which reduced the switching losses of the inverter. The track current was 15 A and the receiver coil current was 27 A, which matched the simulation results. The voltages on the transmitter and receiver resonant tanks were 952 V and 3.6 kV, respectively. Finally, the capacitor bank on the receiver side had the highest voltage stress in the entire system.

**Figure 6. Experimental waveforms of the system operating at 5 kW**

The input voltage was increased from 200 V to 650 V with a constant load value. Figure 7 shows the input and output information as well as the DC-DC efficiency measured by a power analyzer. As shown in Figure 7, power was gradually ramped up from 0.5 kW to 5 kW by increasing the DC input voltage. The efficiency increased from 91.4 to 92.5 percent at the lower power level. The efficiency was kept at 92.5 percent when the output power was more than 2.4 kW. The output power of the W-I coupler-based IPT prototype at 650 V input voltage was 5 kW with a DC-DC efficiency of 92.5 percent.

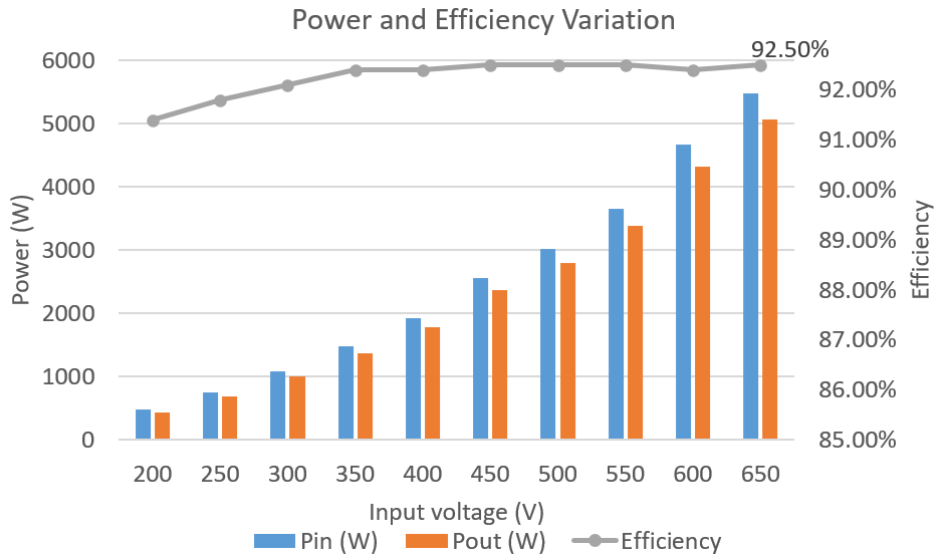


Figure 7. Power and efficiency variation of the IPT testbed

After thorough research of the relevant literature, this appears to be the highest IPT system efficiency for a railway application. The efficiencies in different sections were also measured during the experiment (Figure 8) and based on these measurements, the efficiencies for DC/AC inverter, coupler, and compensation circuit in the rectifier stages at 5kW testing condition were 97.2, 96.5, and 98.6 percent, respectively.

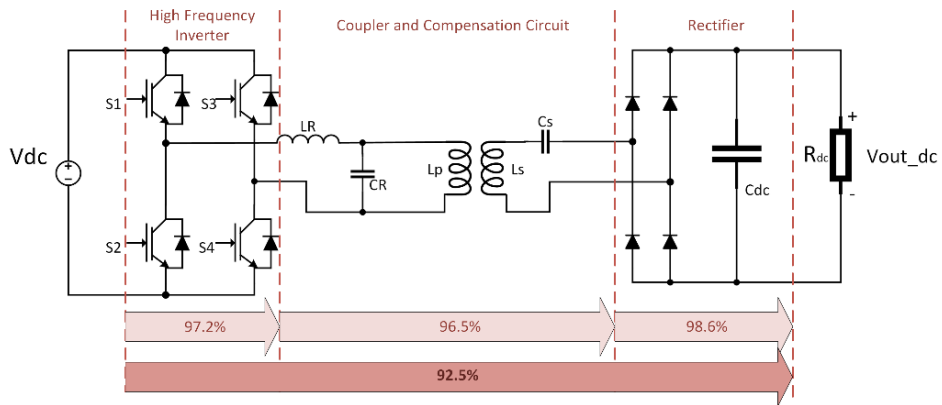


Figure 8. System efficiency measurement results for the IPT prototype

2.3 Packaging Design

The City of Belmont is rebuilding a historical trolley driven by a trailer with an electric vehicle (EV) battery. Figure 9 shows the current state of the trailer. The IPT will provide power for the trailer charger. The packaging design for the IPT includes the receiver, transmitter, and control modules. The receiver module will be hung under the trailer and the transmitter module will be installed between the tracks, while the control module will be placed near the transmitter module. Figure 10 and Figure 11 show the details of the demonstration. The team plans to complete the packaging design and demonstrate the wireless power transfer in the field in Year 2.



Figure 9. Belmont Trolley trailer

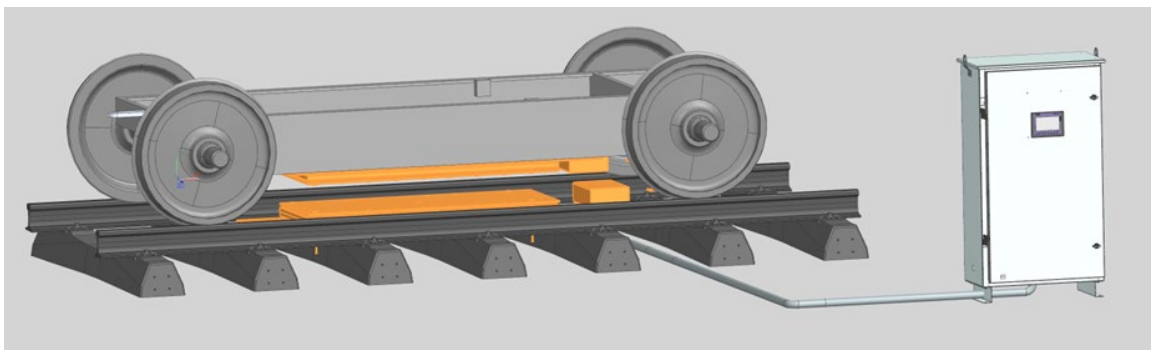


Figure 10. Demonstration diagram



Figure 11. Transmitter and receiver modules and package

3. AI-based Arc Fault Detection

Due to enhanced energy efficiency, improved power quality and reliability, and ease of integration into energy storage systems, DC power supply systems have become popular. However, with the increased use of these power supply systems, electrical safety concerns, especially DC arc faults, have increased in the scientific community. A DC arc fault is dangerous and can cause serious damage to property and personnel. It may cause the temperature to rise to approximately 5,000 °C or above, resulting in fire hazards. Arc faults can be classified as either series or parallel. Parallel arc faults are easier to detect as they produce a current-like short circuit. Series arc faults are more difficult to detect because of a relatively low fault current. Sometimes the nature of different loads, which draw currents like an arc, make the fault detection task more challenging.

Arc faults may happen due to loosened cable connections, faulty cables, trapped cables, and accidentally pierced cables. According to National Electrical Codes (NEC), any DC electrical system requires an arc fault circuit interrupter (AFCI) if it is operating at a voltage greater than or equal to 80 V. The electrical power charging circuitry of the IWPT technology may include additional considerations, such as other power circuits in the locomotives that may induce electrical fire hazards due to arc faults. EV fires, if they occur, are very complex and virtually impossible to extinguish because of the presence of LIBs. This is often marked by a highly toxic vapor cloud along with a hissing noise, possibly followed by an explosion [6]. Therefore, it is essential that the arc faults be detected at the earliest possible time of occurrence to prevent the ensuing electrical fire hazards.

Traditional arc fault detection algorithms, such as Fast Fourier Transform (FFT), Short Time Fourier Transform (STFT), and Wavelet Transform (WT), are based on certain predefined threshold values which are very difficult to define. The predefined threshold value is a limitation as it varies for different systems [7]. Furthermore, the STFT method suffers from window-sized selection, and there is always a compromise between the time resolution and frequency resolution. Conversely, artificial neural network and convolutional neural network-based algorithms have gained increasing attention in various fields due to their excellent performance in classification-related tasks [8].

The objective of this work was to develop an AI-based algorithm which can detect arc fault in the power circuitry at a very high accuracy and at a very early stage of occurrence. The AI-based algorithm should be able to detect an arc fault with an accuracy of more than 99 percent. The overall approach of the task included the development of a system that can generate sustainable DC arc faults and to develop an arc current sensing interfacing board which will read the current data from the system. A good AI algorithm requires a huge database for training purposes. Therefore, a major objective of the project was to collect a substantial amount of arc fault data, to develop an AI algorithm, and to train that AI algorithm with the database. Then, in the real-time electrical system, the current data from the interfacing board can be fed to a microcontroller unit (MCU) where the AI-based arc fault detection algorithm can be pre-implemented. If an arc fault is detected, the MCU sends a trigger signal to the circuit breaker to break the power circuit and isolate the faulty part from the functioning section.

3.1 System Architecture

The system architecture of the IWPT's DC arc fault detection system consists of a DC source (i.e., battery/battery pack), an arc generator to create the arc fault, and an AI-based AFCI (Figure 12). Electrical loads are connected in series with the arc generator. The AFCI has four sub-systems, including an interfacing board, analog to digital converter (ADC), Raspberry PI4 MCU, and trip signal generator. The purpose of the interfacing board is to sense the load current and generate a corresponding analog signal. The Raspberry PI has no ADC function inside of it; therefore, it requires an ADC to convert the analog signal to a digital signal which is then received from the interfacing board. Once an arc fault is detected, the MCU will generate a trip signal to prompt the circuit breaker to isolate the faulty part.

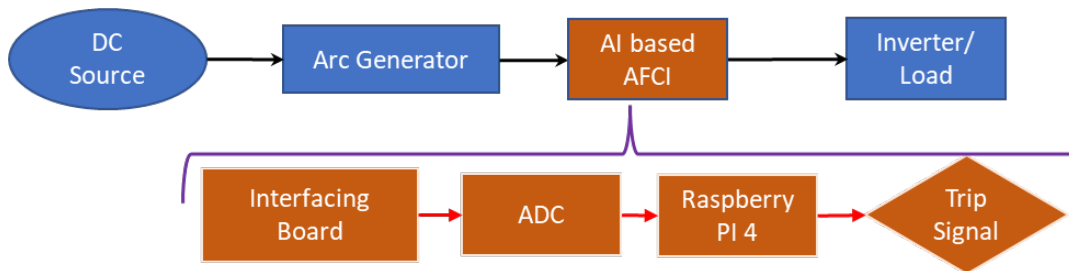


Figure 12. Overall system architecture of the DC arc fault detection system

3.1.1 Arc Generator

Various parts of the system architecture have already been tested in the laboratory. Researchers set up an arc generator and collected sample data for visualization using an oscilloscope. The arc generator (Figure 13) had two arcing electrodes that can be separated using a programmable motor controller that can be set at a desired speed to generate an arc fault. One of the electrodes was made of copper and the other was made of carbon graphite. Both electrodes had a diameter of 0.25 in (6.35 mm). The arc generator was built following the IEC62606 standard and can withstand a maximum of 20 A load current. Using the arc generator, researchers generated a sustainable arc for more than 10 minutes. After generating an arc for a longer period, the electrodes became eroded due to burning and the arcing stopped. Arc generation could be resumed after cleaning the faces of the electrodes with sandpaper. The arc generator contained the arc load bank and a normal load bank where several electrical loads could be connected in parallel as required. The unit was also equipped with a bypass switch to turn off the arcing branch.



Figure 13. Arc generator with arcing electrodes

3.1.2 Signal Conditioning Board

A current sensor was required to sense the arc as well as normal current signals. For this purpose, a signal conditioning/interfacing board (Figure 14) was designed using two current sensors that can sense load currents up to 55 A. The sensor current was then passed through a remote-controlled low-pass filter and then through a buffer circuit using OP-AMP. It was then passed through a clamper circuit. Figure 14 shows the signal conditioning board. A 24 V DC power supply was required as input to operate the current sensors.

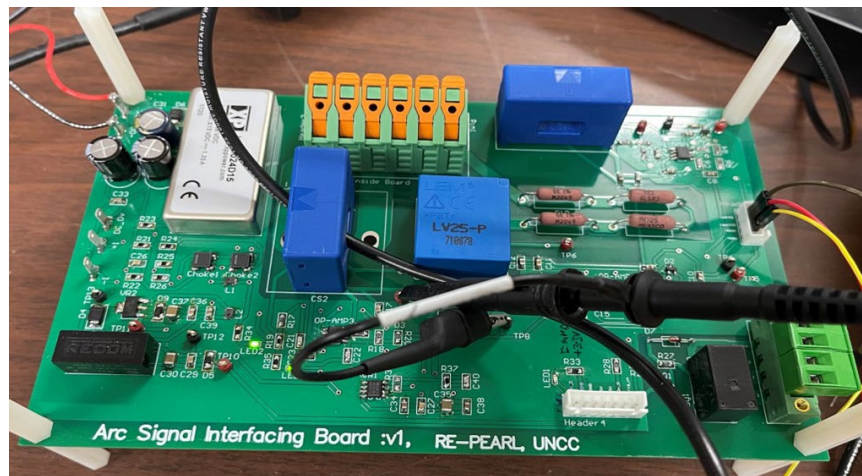


Figure 14. Designed signal conditioning board

3.1.3 Raspberry PI 4B as MCU

For the training of the AI-based algorithm, a high-end GPU machine will be used; however, to develop the algorithm, a low-end MCU was used. For this project, a Raspberry PI 4B was used as a MCU (Figure 15). The Raspberry PI 4B had Broadcom BCM2711, quad-core Cortex-A72 (ARM v8) 64-bit SoC @ 1.5 GHz processor, 4 GB of RAM and 40 GPIO pins. It had the capability to run AI algorithms in real-time.



Figure 15. Raspberry PI 4B

3.2 Arc Generation and Data Collection Using Oscilloscope

Using the arc generator, researchers generated DC arcs using 100 V DC as a power supply source. This DC source was connected to a resistive load of 14.67Ω . The resistors were connected in a series/parallel combination. Figure 16 shows the pictorial view of the arc generation and data collection setup. The arc fault was generated following the UL standard.

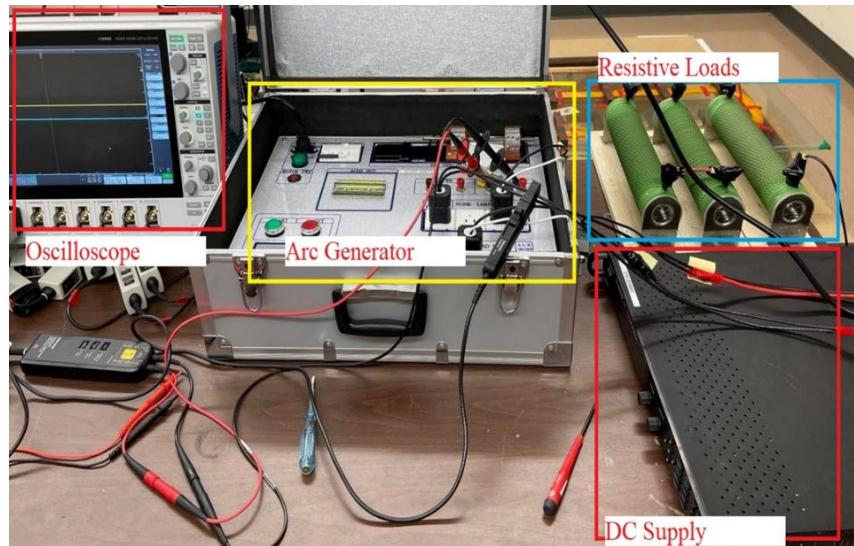


Figure 16. Arc generation and data collection setup with DC power supply and resistive loads

The normal load current of this setup was 6.81 A. During arc generation, the arc current and the voltage across the arc were measured using an oscilloscope. When an arc fault was generated, the current reduced by about 1 A and the voltage across the arc was increased (see Figure 17). Once the electrodes were separated using the motor controller, an arc was started. The arc behaved as a series resistance with the load and researchers noticed a voltage drop across the arc accompanied by a reduction in load current. The arc stopped when the arc gap became large. During the arcing process, an arc may stop momentarily and restrike.

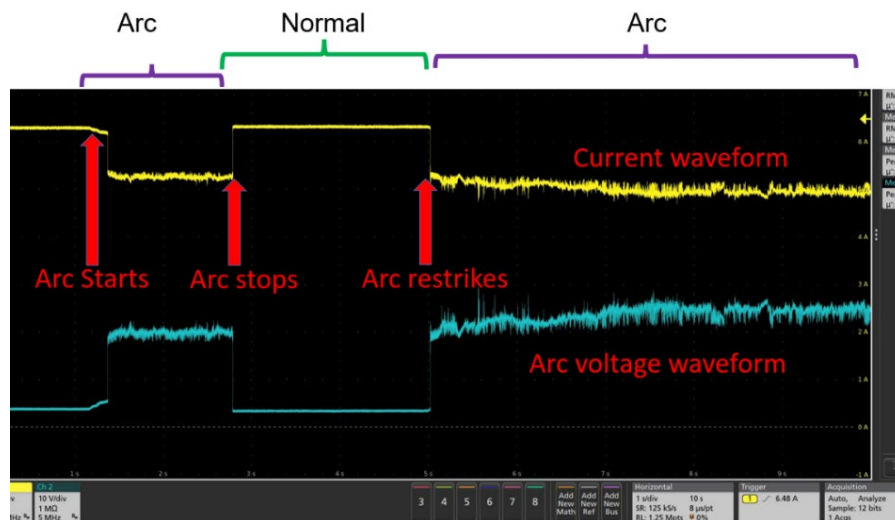


Figure 17. Arc current and arc voltage recorded using oscilloscope

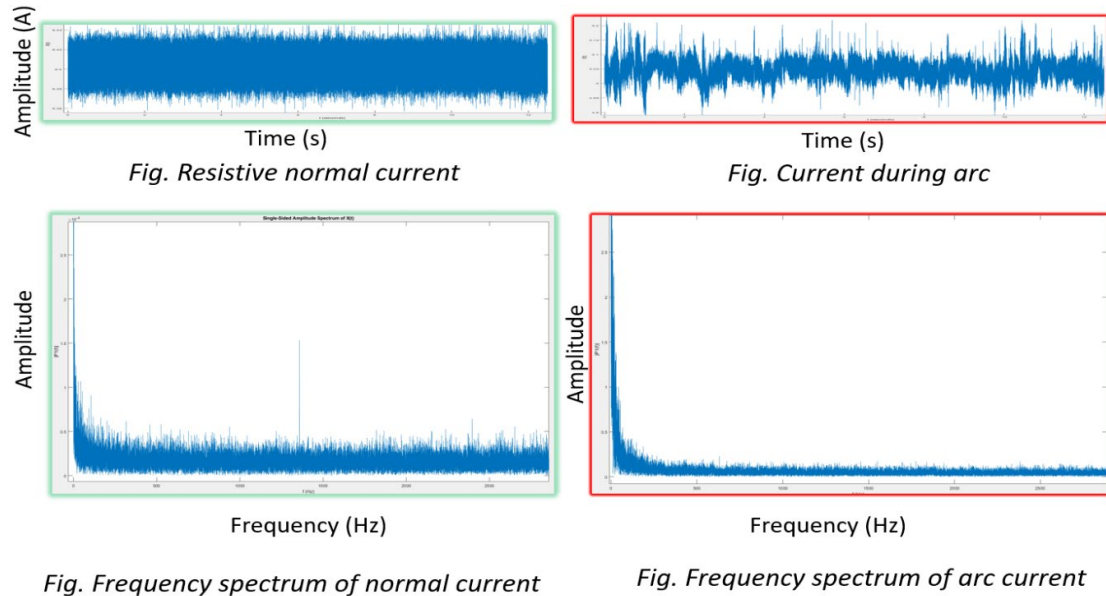


Figure 18. Normal current and arc current FFT

The team performed FFT analysis using the initial set of collected data to determine the differences between arcing and normal frequency spectra (Figure 18). Although a visible difference was noticed between the arcing and normal currents, the difference is subtle in the frequency spectrum. Further analysis is needed to select the frequency range of the spectrum in order to identify the differences between arcing current and normal current. In Year 2, the team plans to complete the development of an arc fault detection prototype and create a real-time, high accuracy, AI-based detection algorithm to improve the electric safety of rolling stocks.

4. Fire Safety Detection

LIB fire and explosion hazards are a major industry concern for both producers and consumers. A better understanding of how LIBs behave leading up to and during explosion/fire events may lead to more effective detection, prevention, and suppression of these events. In almost all cases, LIB fire hazards are caused by short circuiting the battery, which in turn causes thermal runaway (TR). Short circuits can happen externally or internally, but both can be caused by mechanical abuse, defects, high temperatures, and operational abuse [10]. TR occurs when the rate of heat production during LIB operation is faster than the rate of heat dissipation and is generally classifiable when heating occurs at greater than 20 °C/min [11]. Once a state of TR has been entered it typically cannot be stopped or controlled and can cause dangerous side effects such as ejection of gas, shrapnel, or smoke, extreme temperatures, and fire.

LIBs exist in various shapes, arrangements, and chemistries (i.e., design topology). These variables each have their own individual sets of pros and cons. Determining the behavior characteristics of different types of LIBs is paramount in assessing the TR risks involved with each individual battery. This section discusses the development of a wireless battery fire monitoring system that can be used to investigate LIB behavior during battery fire incidences. This fire and explosion detection system (FEDS) will also be used to develop a scale-up system designed to monitor LIB-powered passenger trains during operation.

4.1 Background of LIBs

LIBs can be found in two different cell shapes (i.e., cylindrical and prismatic). A prismatic cell can further be divided into a hard case (i.e., metal or hard plastic) or soft pouch style (i.e., surrounded in a lightweight foil), whereas cylindrical batteries are typically only found in hard metal cases (Figure 19) [12].

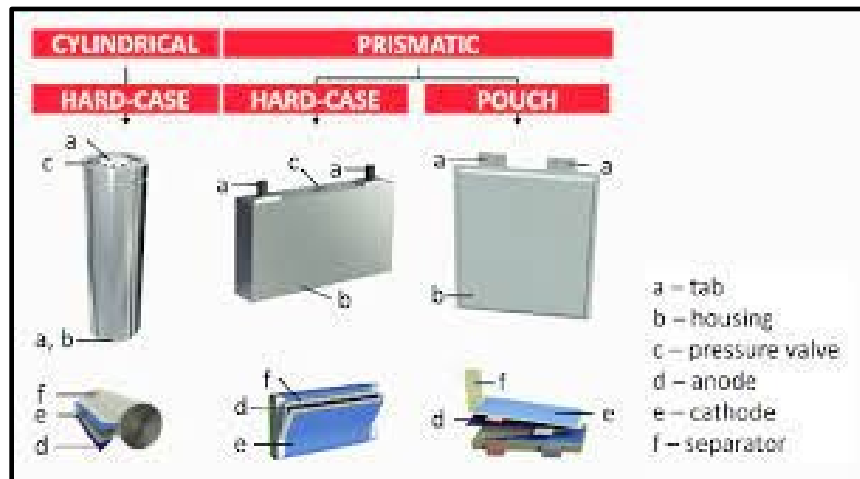


Figure 19. Typical LIB shapes [12]

Prismatic cells in a hard plastic casing are commonly found in cell phones. Each of these individual cell types can be arranged into modules comprised of multiple cells. For instance, Tesla batteries are comprised of 6,831 cylindrical cells [14]. A detailed schematic of typical 18650 cell contents is shown in Figure 20 [14]. Figure 21 shows detailed prismatic schematics [15].

Although some of these cathode chemistries may have advantages in terms of sustainability and high energy density, some may have disadvantages in terms of low TR temperature and high energy release during runaway. Figure 22 shows the results from accelerated rate calorimetry (ARC) of different battery chemistries at a state of charge (SOC) of 100 percent [9].

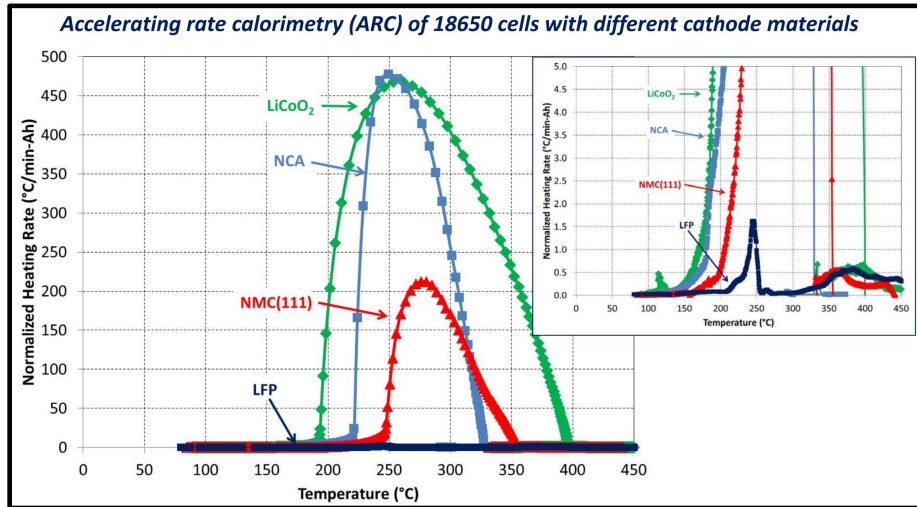


Figure 22. ARC vs. SOC for batteries with different cathode materials [9]

The same study investigated the effect of SOC on TR behavior, which is perhaps the most controllable aspect of any LIB. Figure 23 shows the heating rate versus temperature of the same IMR pouch cells at different SOCs [9]. The scaled-in view shows that when the SOC is higher, the initial heating rate begins higher and rapid increases in heating begin at a lower temperature.

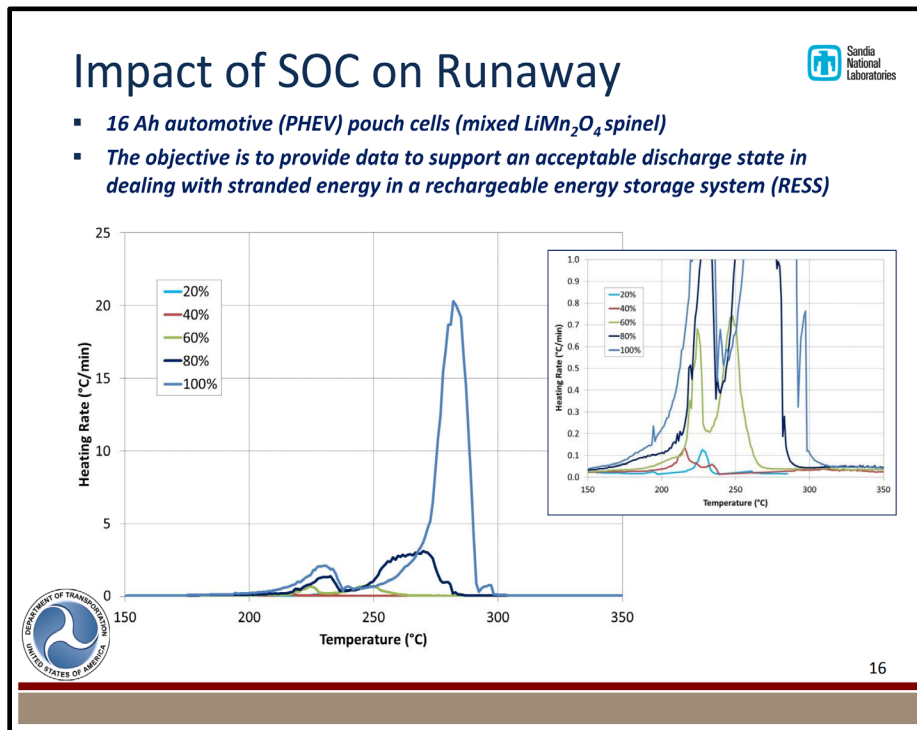


Figure 23. SOC impact on TR in 16 Ah automotive pouch cells [9]

There is an effectively exponential correlation between the maximum heating rate and the SOC (Figure 24). In this figure, a linear relationship is seen between the total release of energy and the SOC [9]. Researchers noted a significant decrease in heating rate roughly 40-60 percent SOC and recommend a standard shipping and handling SOC of approximately 50 percent.

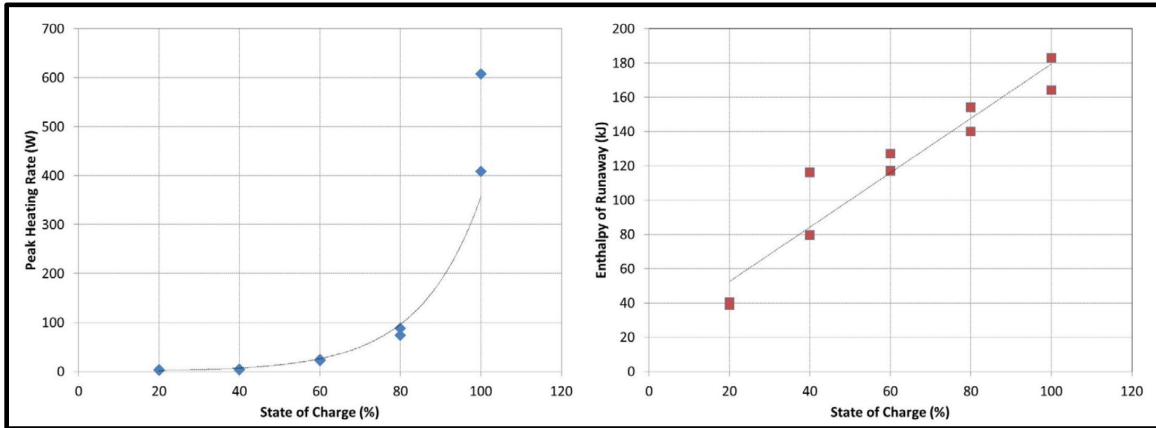


Figure 24. SOC relationships from tested cells [9]

4.2 Fire Safety Approach

Manual short circuiting of the batteries was performed to determine key parameters during the TR of various types of LIBs. LIB external thermal abuse was simulated by placing a LIB on an electric hotplate which caused an internal short circuit (ISC). Multiple LIB chemistries and shapes were investigated along with different SOC within each type. Various forms of wireless data collection were employed during each test including digital video recording, infrared (IR) video recording, on-battery-TC(s), and handheld IR devices (i.e., video thermometer, IR thermometer, and compact IR camera). A schematic of the test system and environment is shown in Figure 25.

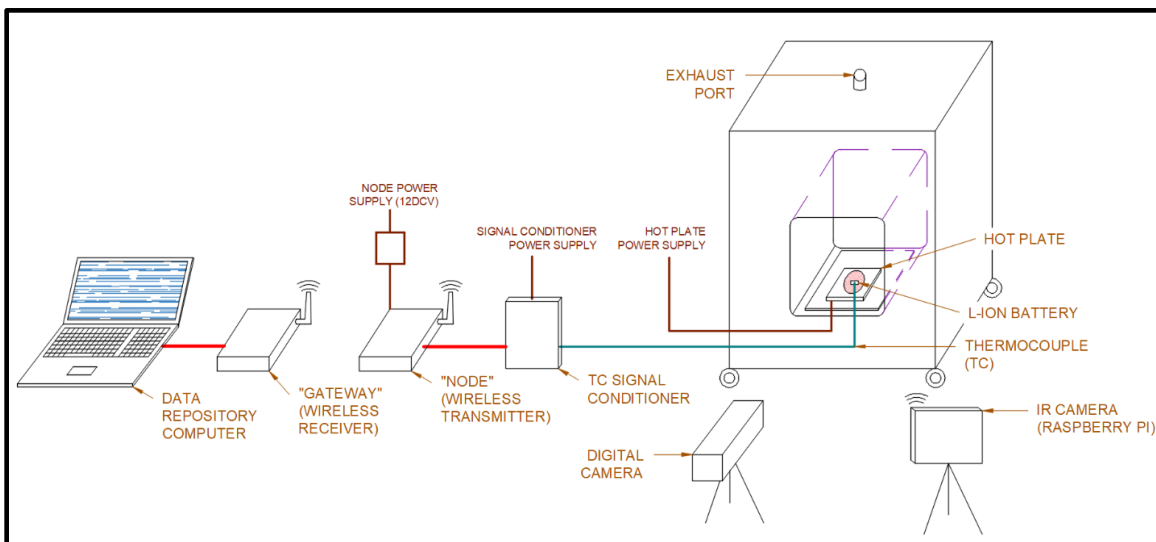


Figure 25. Current test system schematic

All instrument accuracies were validated during initial unreported battery tests and during “dry runs” of the hotplate with no battery. The handheld IR devices are not shown in the schematic as the locations varied while they were used on the hotplate to determine the consistency and magnitude of its heating process, determine temperature of battery remains when TC fell off after explosion events, and spot check temperatures. To confirm and build upon referenced literature, the heating of three battery chemistries (i.e., ICR, IMR, INR) with varying capacities (mAh) and SOC varying between 0-100 percent were evaluated for the following parameters: the occurrence of fire (i.e., ignition and sustained flame), smoke, smell (i.e., gasses), the physical expansion of the cell, pressure release (i.e., piercing of battery), explosion, battery temperature, the time of occurrence, the length of occurrence, the post-test condition of the battery, and the mass lost during fire (when applicable).

The findings from these tests were then used to optimize the electric current system, determine the effectual capacity of test parameters on battery safety, and make recommendations on battery selection and use, especially in the planning of train applications.

It should be noted that the original FEDS prototype design included gas sensors but the initial gas detection instruments could not be validated for accuracy. Therefore, subsequent testing continued without gas detection. Researchers discussed future plans for a possible gas-to-bag collection system. These bags could be analyzed in detail after the test.

4.3 Technical Results

The overall battery testing approach is shown in [Figure 26](#). Researchers used an intermediate-sized box furnace as a test chamber to contain flames and smoke and an electric hotplate was placed inside the box furnace and used as a temperature source for thermal abuse of the batteries. Various instruments were used to record the temperatures of the battery and the hotplate. A laptop was used for data acquisition and data processing.

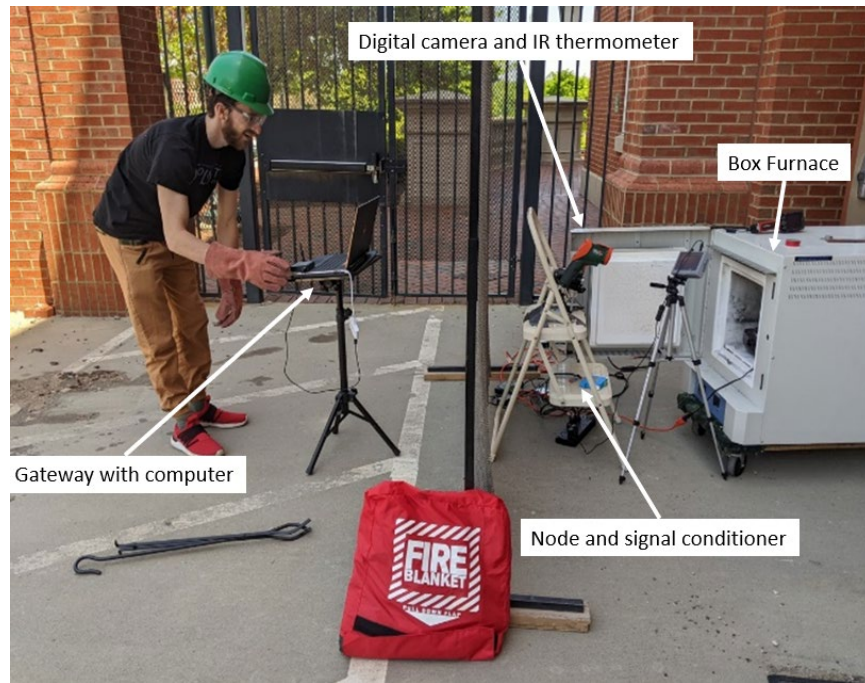


Figure 26. Candid test shot with PPE

Tests were performed inside a Thermo Scientific™ box furnace with a ceramic fiber interior capable of withstanding high temperatures. The door was left open during testing to allow for clear views of the image recording devices at a safe distance. A dimensioned schematic of the box furnace is shown in [Figure 27](#).

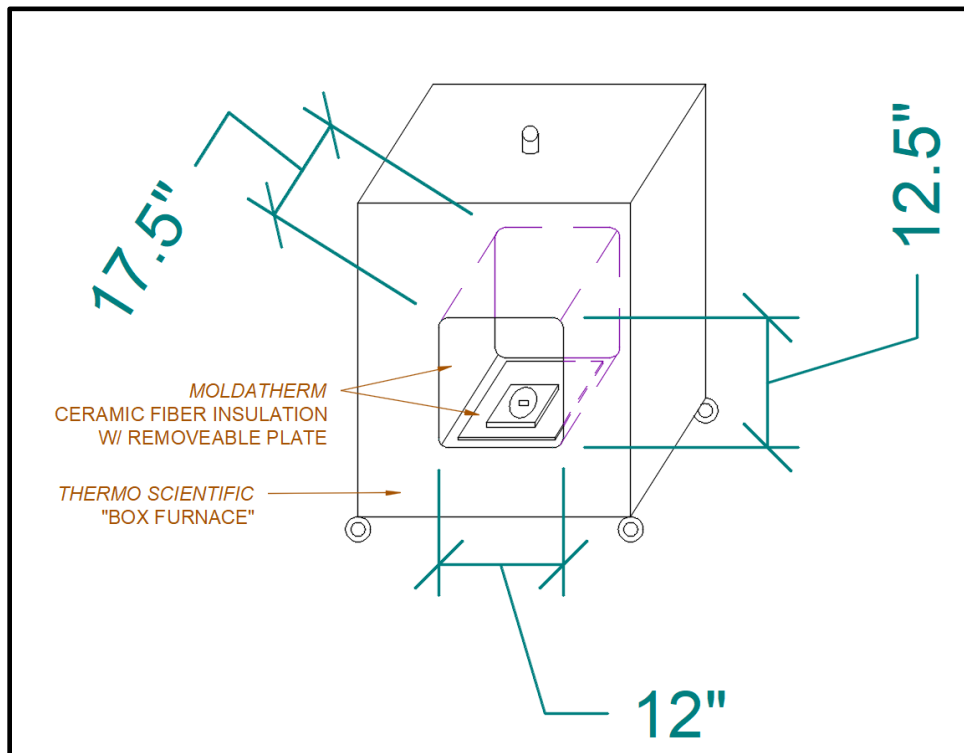


Figure 27. Test box furnace detail

Safe practices at the fire site were performed including nearby personal protective equipment (PPE) and fire/projectile barricades.

4.4 Experimental Methods

In each battery test, a LIB was placed directly on the hot spot of the hotplate which was then turned to its highest setting upon activation of sensors. The hot spot of the hotplate was determined using thermal imaging. By analyzing the data logged by an IR thermometer aimed at the hot spot for multiple ambient-to-active heating sessions of the plate, the hotplate was determined to heat consistently every time. Plate heating data was continually collected for nearly every reported test to monitor the hotplate for depreciation in heat output over time and to develop a rolling average heating curve that was adjusted for outliers. An average reading was also taken to alleviate minor differences in the IR gun laser location from test to test, though it was not as difficult to ensure contact with the plate hot spot for the larger battery. For this reason, when any reported results referenced the hotplate temperature, a rolling average was used instead of the IR gun results for that test. A plot of the individual tests' hotplate heat vs. time curve and the average is shown in [Figure 28](#).

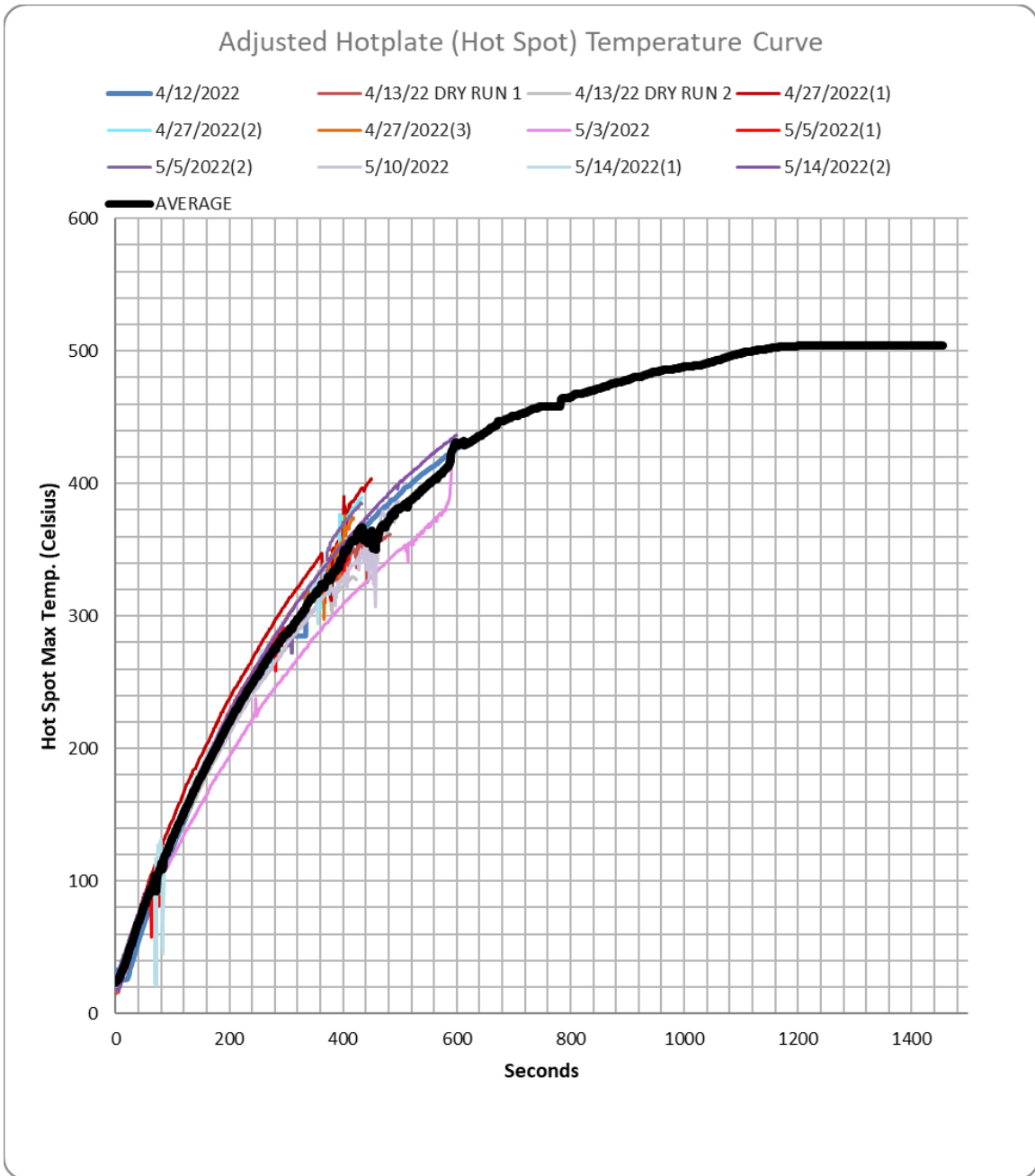


Figure 28. Adjusted hotplate mean heating curve

The hotplate was usually turned off shortly after the battery was ejected from the plate surface, which resulted in different lengths of heating respectively. Nonetheless, a consistent shape and magnitude was seen in all tests performed. Between immediately successive tests, a metal tray filled with ice was used to bring the hotplate down to ambient temperature in a reasonable amount of time. A dimensioned schematic of the hotplate is shown in [Figure 29](#).

The rest of the testing system was established based on the anticipation of future applications intended in battery locomotive designs including TC and IR video recorder. Real-time gas and smoke detectors have also been proposed for train use.

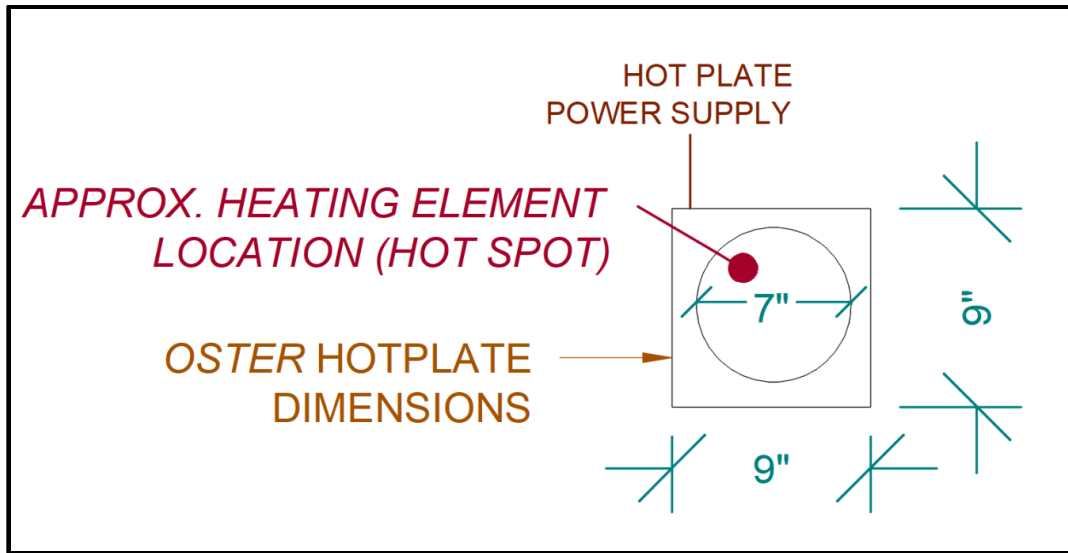


Figure 29. Hotplate detail with hot spot

Testing originally began with a larger TC but was changed to a smaller TC designed for surface application, resulting in more accurate results. All reported tests used an Omega type-K surface coupler taped to the opposite side of the battery touching the hotplate (excluding the single May 3, 2022, 18650 cell test) with thermal resistant tape that can withstand up to 80 °C. The TC sensor was validated by comparing its thermal readings to two IR guns (i.e., green EXTECH, red FLIR) and a handheld FLIR thermal imaging camera. All four devices reported the same temperature on both the heated hotplate and a human body within reasonable degrees of deviation. The TC was connected to an Omega signal conditioner which translated the TC signal for the “node” device to which it was wired. The node acts as a router which transmits all data to the “gateway” device located a safe distance away. The gateway is connected to the monitoring computer where SmartConnect software records and displays the data in real-time. While the gas sensors that were used initially proved to be ineffective, they were able to connect directly to the node which is currently capable of receiving 8 separate sensors. The 2-in-1 (CO, CO₂) gas sensor required its own power supply as did the conditioner and node. In theory, this system could be expanded to include more sensors and configured to be powered by the same batteries it is monitoring.

The IR video recorder is currently a separate system from the TC system. The IR camera is connected to a tablet that operates on a Raspberry PI board with wi-fi capabilities. On the same monitoring computer used with the TC, a remote desktop connection can be made to the IR camera device so the video image can be seen and recorded at the same time as the TC data. Currently the remote desktop connection window is being recorded using Open Broadcaster software. Using C++ programming to execute the thermal recording has proven to be most efficient. When attempting to validate the readings from the IR camera, it was noticed that the device consistently reads a lower temperature than all other devices and TC (the difference ranges from 30-90 °C). The low resolution of this prototype IR camera is understood to be the cause for this difference; however, it has been used in every reported test. In the future, these thermal images may still be used for image processing and/or be adjusted for accuracy. Its images were occasionally used when TC fell off the battery, but the fire event remained in the IR

camera's view for a rough estimation of event temperature. A first-person, functional view of the TC/IR camera system is shown in [Figure 30](#).

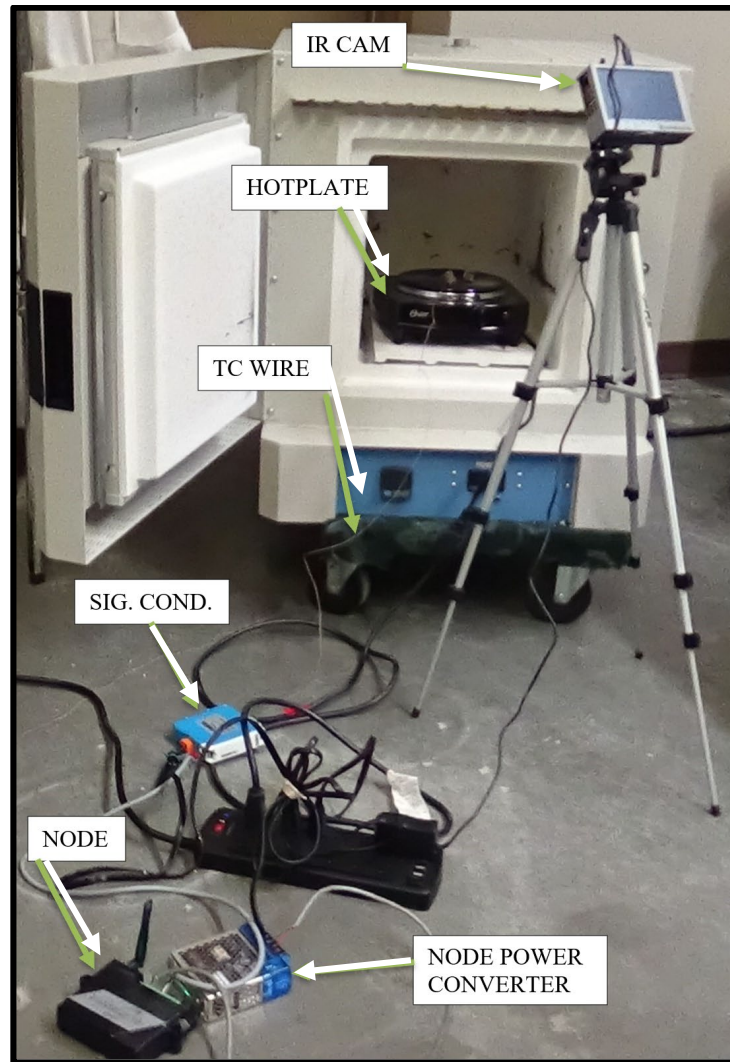


Figure 30. POV of wireless system

In this research, 17 batteries were tested for reporting comprised of:

- 5 ICR (LCO) – Hard-plastic prisms with SOC of 0, 50, 75, 100, and 100 percent
- 5 IMR (LM) – Cylindrical 18650s with SOC of 0, 60, 60, 80, and 100 percent
- 7 INR (NMC) – Cylindrical 18650s with SOC of 0, and 6x100 percent
 - *One of these seven tests was performed with endcap on plate surface*

All batteries tested were used batteries donated from local battery stores. Only batteries that showed SOC and the ability to increase SOC were used. Two “universal” chargers were used to determine an approximate SOC and bring batteries to certain SOC when desired. One charger worked for the prismatic LCOs, with SOC increments of 25 percent, and the other charger worked for both cylindrical chemistries with SOC increments of 20 percent. These chargers are shown in in [Figure 31](#) and [Figure 32](#).

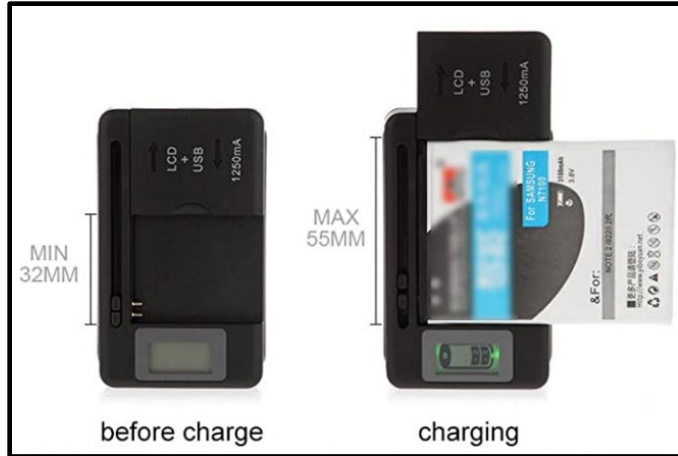


Figure 31. Rijer prismatic charger



Figure 32. EASTSHINE cylinder charger

TC was placed in the middle of the opposing plate-face of the battery (excluding one endcap test). Typical placement of these batteries can be seen in [Figure 33](#) through [Figure 35](#). During every reported test the hotplate was turned to the highest setting.



Figure 33. Pre-heating prism (LCO) placement



Figure 34. Standard 18650 cell placement



Figure 35. Endcap placement (May 3, 2022)

4.5 Results and Observations

Recorded videos were replayed to determine the pertinent visual identifiers of TR in each test. The time of occurrence of the critical events was compared to the average temperature of the hotplate and the top-of-battery temperature at that time. When applicable, the length and appearance of visual identifiers was also recorded (e.g., the length of time a battery was on fire). When available, the temperature of the battery directly after fire/explosion was recorded along with the mass of material burned or ejected from the batteries. Descriptions of the remaining battery pieces were made and pictures were taken of the events. This combination of data and observations has been formatted into a large test matrix. For convenience and efficiency this matrix has been broken down to highlight key findings.

4.6 Sample Cylindrical Cell Battery Behavior

Figure 36 shows an example of the TC temperature curve for an 18650 battery with 100 percent SOC plotted over time from hotplate activation. The first rapid spike in temperature signifies the time of an explosion event, which in this case was a rapid explosion of sparks that caused a gash down the side of the battery near the positive side endcap (see Figure 27). The battery became red hot for over a minute and reached a temperature of 755 °C. In this instance the TC was less than 1/2 inch away from the burning battery, which became lodged between the hotplate and the ceramic wall, allowing a fraction of the TC tape to remain in contact with the battery for a few seconds and then come off the hotplate. The TC was surrounded by the tape in the same location. While the battery appeared to be red hot, the only visible flames were that of the burning tape which lasted just under 1 minute. When the TC data is viewed alongside the video, the approximate 440-445 seconds TC point coincides with the extinguishing of the tape flames; this leads to the rapid drop in the ambient outdoor temperature that day, which also validates the response and accuracy of the TC. Video stills marking these observations are shown in Figure 38 and Figure 39.

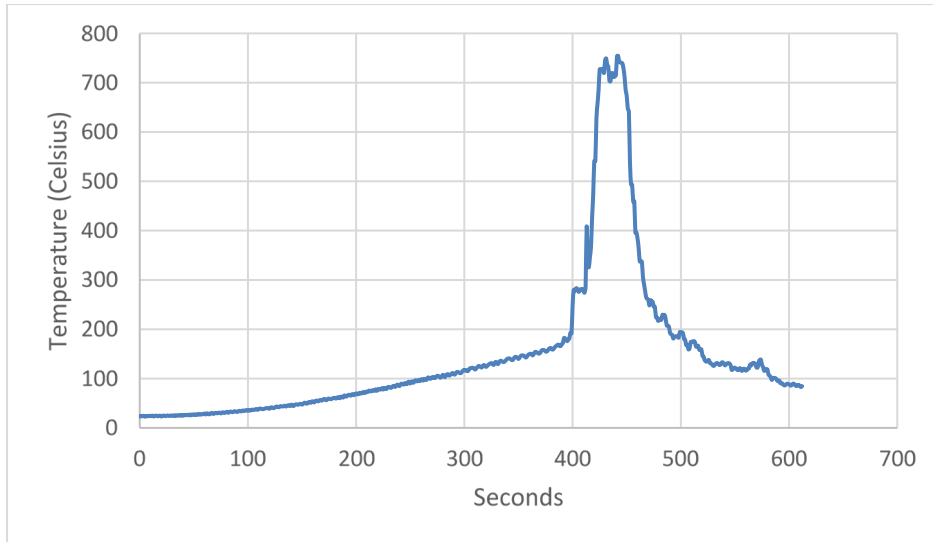


Figure 36. 18650 cell INR 100 percent 2,600 mAh (April 27, 2022, Test #3)



Figure 37. Post-test condition (April 27, 2022, Test #3)



Figure 38. ~5 seconds after explosion (April 27, 2022, Test #3)

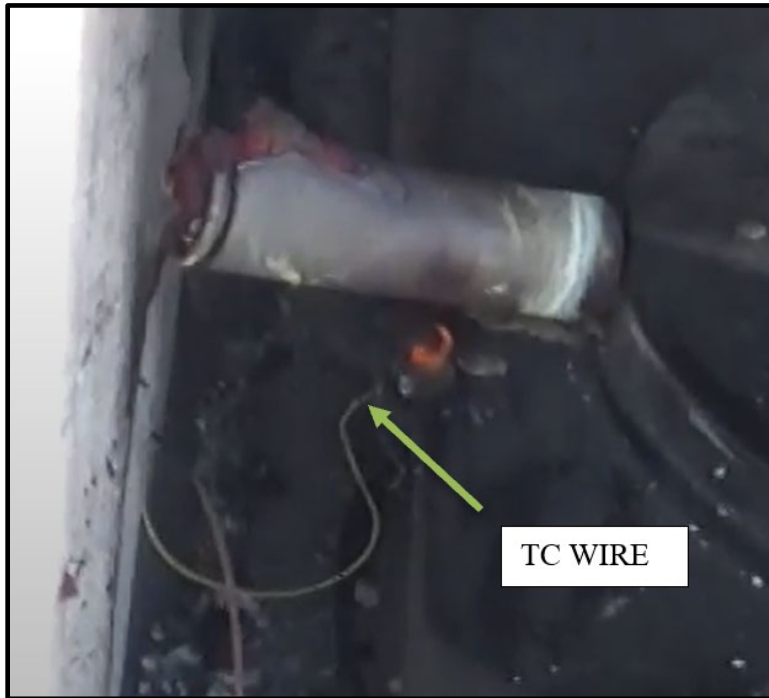


Figure 39. ~50 seconds after explosion (April 27, 2022, Test #3)

Approximately 1.25 minutes after the explosion, the IR thermometer being used to monitor plate heating was moved to the surface of the battery once it was deemed safe to do so. The laser sights were pointed at the middle of the length of the battery and read an initial maximum temperature of 359 °C, while the sights that were pointed at the “gash end” of the battery briefly read a temperature of 481 °C. At 2.75 minutes after the placement of the IR video thermometer, the battery had cooled to 110 °C, but at this point the battery was removed from the box furnace. In most tests an attempt was made with various handheld thermal devices to record the temperature of any pieces of the battery that remained. In many instances, the capacity range of the available devices was exceeded.

IR camera recording stills are shown in [Figure 40](#) and [Figure 41](#), capturing the second before explosion and the second after explosion, respectively. In subsequent seconds, the IR camera read a maximum temperature of 518 °C for a split-second but then immediately dropped below 400 °C and hovered around 300 °C for the remaining two minutes of video.

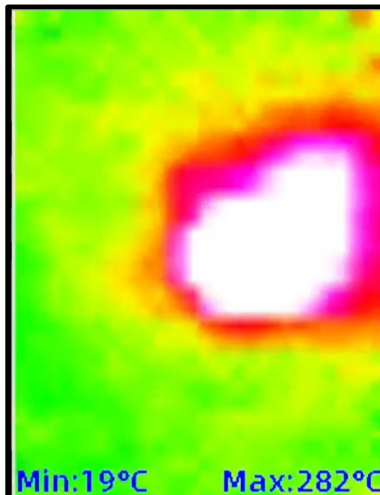


Figure 40. 1 Sec. pre-expl. (April 27, 2022, Test #3)

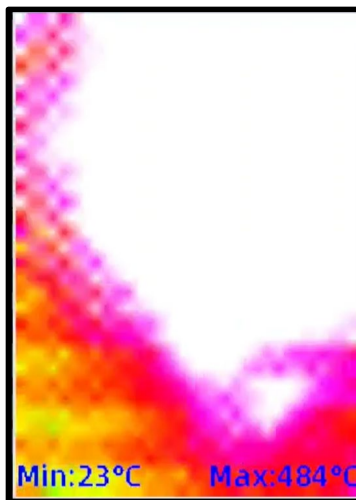


Figure 41. 1 Sec. post-expl. (April 27, 2022, Test #3)

4.7 Comparison of Results

4.7.1 Combined TR Temperature and Time

Due to variability in the time and distance, TC was displaced from the battery from test to test. The data for each test ended at the point of explosion/hissing/expansion that indicated TR, categorized by chemistry and plotted for comparison within each category. This process helps keep plots concise and highlights the time and temperature of the most active stage of TR. These comparisons are shown in [Figure 42](#) for all LCO tests, [Figure 43](#) for all IMR tests, and [Figure 44](#) for all INR tests.

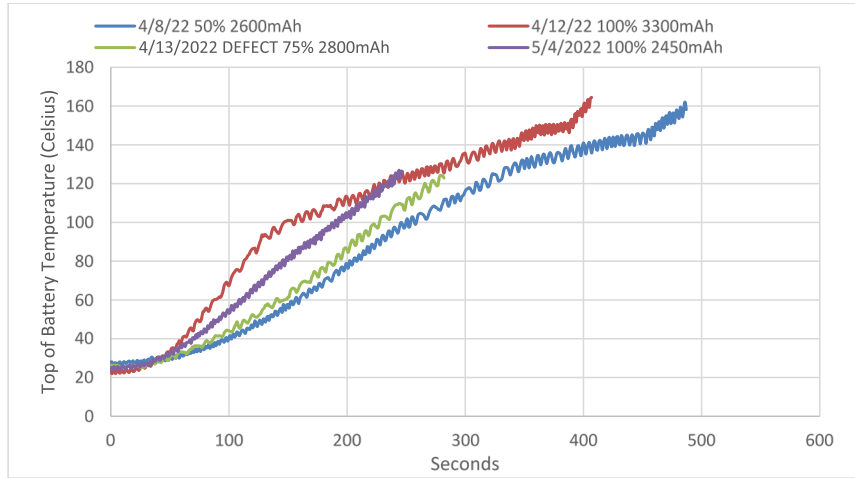


Figure 42. Prismatic LCO TR temp vs. time

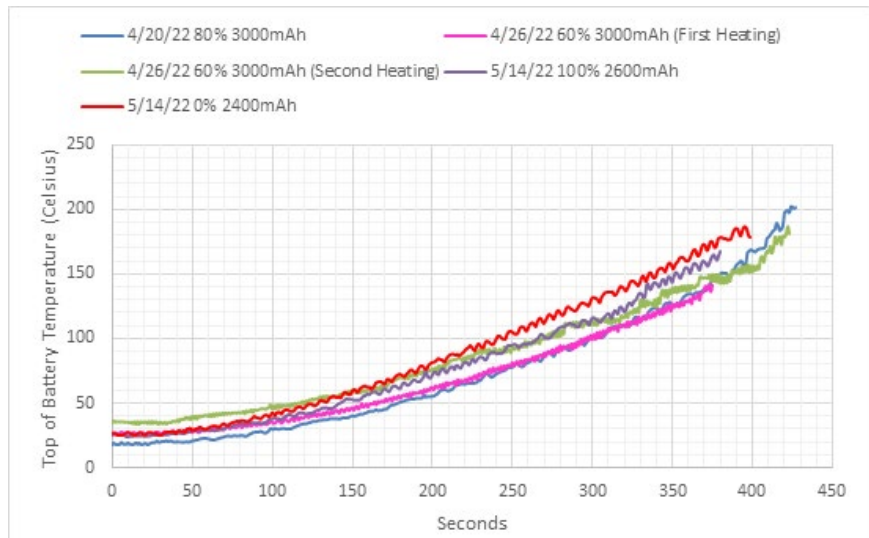


Figure 43. 18650 IMR TR temp vs. time

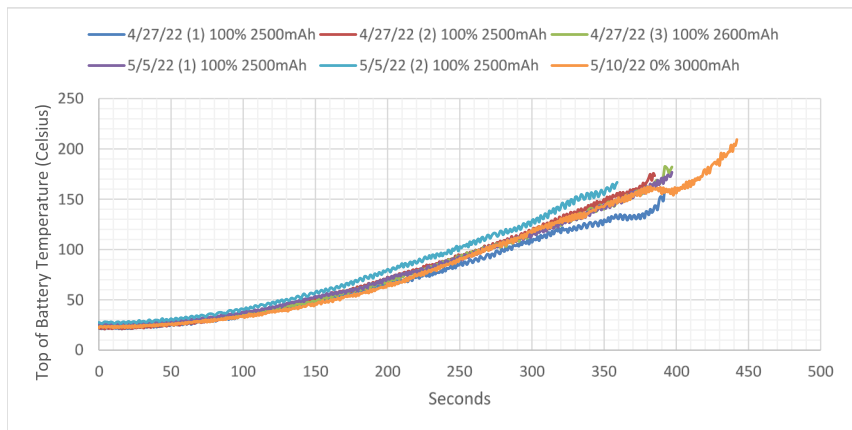


Figure 44. 18650 INR TR temp vs. time

4.7.2 SOC Comparison

Of the three 0 percent SOC batteries tested, only one caught fire, and the duration of fire was short (approximately 2 seconds). The 60 percent SOC from April 26, 2022, was heated until a pressure release pushed it off the hotplate, but no fire occurred. After cooling to near ambient temperature, it was placed back on the hotplate until a pressure “hiss” occurred again and at a higher temperature and longer time. Again, there was no fire.

When analyzing the key indicators of “visible smoke” and “audible hissing” among the IMR batteries, the 0 percent SOC battery sustained higher temperatures and longer times for “smoke” and “hiss” to occur, respectively. Conversely, the 100 percent SOC IMR showed the same indicators at both lower temperatures and shorter times. A gradual decrease in temperature and time can be seen as SOC increases between 0-100 percent. Details of these findings are shown in [Table 3](#).

Table 3. IMR SOC Comparison

TBL 1	ALL TEMPS (C°) ALL TIME (sec)	S.O.C.	SMOKE/SMELL			PRESSURE RELEASE (HISS)		
			PLATE TEMP	BATTERY TEMP	TIME	PLATE TEMP	BATTERY TEMP	TIME
18650 IMR (NM)	<u>4.20.22</u>	80	328	150	382	328	146	375
	<u>4.26.22 (1ST HEATING)</u>	60	328	141	375	328	141	375
	<u>4.26.22 (2ND HEATING)</u>	60	316	140	350	360	181	424
	<u>5.14.22</u>	100	304	131	332	304	131	332
	<u>5.14.22</u>	0	324	167	363	337	184	390

4.7.3 LCO Behavior

According to the characteristics of temperature curves and video recordings, the TR and thermal abuse behaviors of LCO (i.e., ICR) lithium-ion prismatic cells can be divided into five stages: cell swelling, pressure release, explosion, stable combustion, and flame burnout. Prismatic cells can be seen progressing from the original thin and flat prismatic to a bulging shape. Eventually the swelling stopped and the internal pressure caused the cell to rupture. Cells often began to hiss while releasing a large amount of white smoke. Eventually the temperature increase caused rapid expansion and explosion of the battery. Prismatic batteries were observed to fail at one or both endcaps or the entire battery was shred open. Typically fire events followed explosions with the exception of the tests with 0 percent SOC. Battery fire cannot be confirmed in the April 8, 2022, test (i.e., battery with 50 percent SOC) due to the large release of heavy white smoke during and after the explosion. In cases where the endcaps were blown off, an audible jet of flames occurred momentarily before the battery was engulfed in flames. When the battery shred, immediate engulfing occurred. After a few seconds the cell typically entered a stable combustion stage with a maximum recorded time of 165 seconds (May 4, 2022). With the rapid consumption of the combustible components, the flames gradually weakened and extinguished. Not every stage was guaranteed to occur; also, large swelling, pressure release, and combustion can happen together in a fraction of a second.

4.7.4 18650 Cell Behavior

While a small amount of expansion is likely present in 18650 cell heating, it is not visible to the human eye with current test methods. All other stages described for LCO batteries were present

with the 18650 cells. In all 18650 cell tests, pressure was released and casing integrity failure occurred first at the positive endcap. In most cases, as TR progressed into an explosion, the positive end of the battery casings blew off or the entire case shredded. Only in one case did both endcaps fail, and in another case a gash appeared in the side of the battery with the overall shape still intact, as mentioned previously. However, these are only isolated cases.

All tests in which an 18650 cell rapidly escaped the test chamber and travelled a significant distance were conducted using 100 percent SOC batteries. The 18650 INR battery (May 3, 2022) tested on its endcap took longer to reach its reaction temperature of 162 °C, but its explosion caused the battery to shoot approximately 35 ft from the test area, skipping along an exterior wall which it charred once it stopped moving. The battery would have likely sustained its integrity further if the wall was not present.

4.7.5 Chemistry Comparison

Table 4 shows the average plate and battery temperature and time to occurrence of key indicator stages in TR/thermal abuse behavior within the three tested chemistries. All applicable tests were included in determining the average regardless of SOC. If a certain indicator did not occur during one test, it was not considered in determining the shown average; however, the same battery may have experienced a different indicator, and would have been used for calculating that respective average.

Table 4. Intra-Chemistry Indicator Averages

INTRA-CHEMISTRY	EXPANSION			SMOKE/SMELL		PRESSURE RELEASE (HISS)			EXPLOSION			FIRE	
	AVERAGES	FIRST SIGN TIME	TIME-TO-MAX	PLATE TEMP	BATTERY TEMP	TIME	PLATE TEMP	BATTERY TEMP	TIME	PLATE TEMP	BATTERY TEMP	TIME	LENGTH
ALL TEMPS (C°)	ICR	136.8	325.5	262.0	114.0	254.5	263.5	127.3	298.3	292.0	143.8	355.8	75.7
ALL TIME	IMR	-	-	320.0	145.8	360.4	331.4	156.6	379.2	341.0	184.0	403.5	2.0
(sec)	INR	-	-	284.8	120.3	299.5	303.8	129.6	330.0	335.2	170.4	386.4	19.4

Table 4 Notes:

- Expansion of 18650 cells is not visibly identifiable during heating to human eye.
- Only 2 IMR batteries caught fire, while 5 IMR's were used in other averages, including the second heating of the 4/26/22 test.
- All INR batteries are 100% SOC.

In cases where the inner contents of the battery were exposed or separated from the battery casing when taking post explosion/fire temperatures, the contents were consistently observed to be hotter than the casing of the battery. For instance, on the first May 5, 2022, test, the battery contents were recorded to be over 400 °C less than a minute following the explosion, while the separated/shredded casing was recorded at 235 °C. In tests where the battery contents separated from the casing, the circular layers either remained together or spread apart into individual layer leaflets. High temperatures and flames were only found when the contents remained intact, compared to the rapidly cooled pieces when spread out. The metal 18650 cell casing was never observed to be burning, while the plastic LCO casing often was. Nothing from the inside of the battery was ejected that had notable weight or force in terms of projectile impact hazards.

4.8 Summary

In tests performed alongside the TR observations, especially during thermal abuse [16] [17], high temperatures are believed to initiate with the decomposition of the solid electrolyte interphase

layer which releases heat at around 80 °C [16], combined with increasing hotplate temperatures. The battery separator eventually melts between 150-200 °C [17], and the migration of electrolyte caused an ISC and TR in the already hot battery [16]. This often causes an explosion or fire event. The average temperature of the explosion for the 18650s occurs soon after this separator melting temperature range is reached. The average temperature for the prismatic LCO batteries is just below this range but is explained due to the faster heating rate seen through the hard-plastic casing and the reported lower TR onset temperatures for LCO chemistries [12].

There is a noticeable effect on the occurrence, severity, and length of fire events due to SOC. As expected, lower SOC LIBs possess less stored energy, which typically correlates to a higher temperature needed to create smaller energy hazards. Dangerous conditions can occur no matter the SOC. In all instances, the dangerous conditions that were considered included (but were not limited to) high temperature propagation, toxic fumes/smoke, sustained fires, and dispersion of embers and high temperature projectiles. When possible, it is recommended that LIBs be kept at the lowest possible SOC that still allows for efficient charging requirements. Ideally batteries should not be fully discharged or charged over 60 percent.

Observed LCO battery hazards include heavier white smoke and more fumes typically than 18650s, prismatic cells not displacing nearly the same distance or with the same force as 18650s, and longer sustained fires being more prevalent (seen in averages within chemistries and maximum burn times).

Failure in the 18650 cells was always noticed first at the positive endcap due to the presence of safety vents functioning as designed. As pressure build-up exceeds the pressure release rate of safety vents, these vents appear to become weak spots in the casing surface which nearly always causes the internal combustion to eject out of the positive end. The tests in which the IMR case endcap remained intact was likely due to the low SOC (i.e., 0 percent, 60 percent) producing less pressure during heating. In the detailed April 27, 2022, INR test, the positive end plate became lodged against the wall before it could be fully removed; in this case the pressure had to be released out of the corner and along the side near the end plate, causing a gash. In the only case where both endcaps were blown off (May 1, 2022, Test #1) the result likely occurred because a 100 percent SOC battery was used. The elements combusting were the contents of the 18650 cells; when these contents escaped from the casing during rupture, they were able to start fires within an estimated radius of 10 ft, although only if the contents stayed intact enough to hold high temperatures. When the rupture size of the casing was small or contained to just the endcap, this created a jet-like propulsion of the battery; in this case the estimated fire danger radius could be over 50 ft. This weak spot revealed in 18650s should be considered when designing a module or pack of cells, and researchers recommend positive endcaps be prevented or limited from pointing toward other batteries. To ensure safety, future tests of a similar nature should use a large, contained space that allows for video recording but can still contain any projectile batteries. Having multiple high-speed camera angles with a measured “checkerboard” background in view of each camera would make it possible to accurately determine the projectile velocity.

A Sandia National Laboratories study that used manual crushing to reduce TR in a battery multi-pack found maximum temperatures of the 11 cells ranging between approximately 450 – 900 °C [18]. This was based on tests where the TC stayed intact to the cell (April 8, 2022) and the other TC was within 1/2 inch from the cell surrounded by burning tape (April 27, 2022, Test #3), resulting in a maximum recorded temperature of 519 °C and 755 °C, respectively. It can be

assumed that most of the recorded TR events that caused explosions or fires reached a similar range of temperatures. The multiple post-explosion readings that maxed out the FLIR IR thermometer (i.e., 360 °C) and FLIR IR camera (i.e., 410 °C) further support this claim.

More tests should be conducted to gain a more even spread of SOC across all three chemistries; 20 – 40 percent SOC tests are planned. A more consistent spread of different states of charge will lead to a more statistically confident test matrix.

5. Conclusion

This project proposed the use of IWPT technology for power charging. This approach focused on the development and integration of three key technologies, including a wireless power transfer system, AI-based arc fault detection, and fire safety detection.

In Year 1, the team completed the IPT prototype development and validated the 5 kW power transfer at TRL 4. The prototype achieved an impressive efficiency of 92.5 percent DC-DC, which is the highest efficiency for rail applications reported in available literature. The team began arc fault detection platform development and was able to collect initial data for future AI-based algorithm development. The team also developed a functioning wireless battery FEDS and performed fire testing on several 18650 and small pouch batteries. All technical deliverables in Year 1 were completed on time. The main conclusions are presented below.

- An IPT prototype for railway application has been completed. Based on the constraints and requirements of railway applications, a W-I coupler was proposed and optimized to wirelessly charge the rail locomotives. The prototype of the W-I coupler-based IPT prototype was validated at 5 kW with 92.5 percent DC-DC efficiency, which is the highest IPT system efficiency reported for a railway application. The packaging design of the IPT testbed is ongoing. In Year 2, the team plans to complete system packaging design, demonstrate 5 kW power charging in the field, and integrate the proposed fault detection intelligence with the IWPT system.
- An arc generation unit which can generate sustainable arc for more than 10 minutes was set up successfully. Arc fault data were collected and visualized using an oscilloscope and differences were observed. The FFT analysis also indicated the differences between normal and arc fault signals. A signal conditioning/interfaces board was designed to sense the current signal for real-time testing. Future work in Year 2 includes planning for the collection of massive arc fault data and the development of an AI-based algorithm for arc fault detection.
- In Year 1, the research team developed a functioning wireless battery FEDS that is currently comprised of a battery surface TC and an IR video camera. The team also performed fire testing on several 18650 and small pouch batteries. Initial findings showed that the SOC has an inverse relationship to the duration and energy of TR effects in thermal abuse tests. These findings led to a recommendation of keeping any type of LIB below 60 percent SOC while also ensuring the batteries are not fully discharged. Improper charge/discharge operation can cause TR, but in a much less visible way than thermal abuse. Looking ahead, the research team plans to integrate gas and voltage sensors into the experimental setup, test mid-sized (i.e., laptop-sized) batteries, and develop prediction tools for battery fire diagnosis. The additional LIB tests and a more evenly spread number of specific SOC increments will lead to a higher statistical significance for the test results and greater confidence in conclusions made from these results.

6. References

- [1] Patil, D., McDonough, M. K., Miller, J. M., Fahimi, B., & Balsara, P. T. (2018). [Wireless Power Transfer for Vehicular Applications: Overview and challenges](#). *IEEE Transactions on Transportation Electrification*, 4(1), 3–37.
- [2] Feng, H., Tavakoli, R., Onar, O. C., & Pantic, Z. (2020). [Advances in high-power wireless charging systems: Overview and design considerations](#). *IEEE Transactions on Transportation Electrification*, 6(3), 886–919.
- [3] Choi, S. Y., Gu, B. W., Jeong, S. Y., & Rim, C. T. (2015). [Advances in wireless power transfer systems for roadway-powered electric vehicles](#). *IEEE Journal of Emerging and Selected Topics in Power Electronics*, 3(1), 18–36.
- [4] Brecher, A., & Arthur, D. (2014, August). [Review and Evaluation of Wireless Power Transfer \(WPT\) for Electric Transit Applications](#) (FTA Report No. 0060). US Department of Transportation.
- [5] Covic, G. A., & Boys, J. T. (2013). [Modern trends in inductive power transfer for Transportation Applications](#). *IEEE Journal of Emerging and Selected Topics in Power Electronics*, 1(1), 28–41.
- [6] [What are the fire risks of electric vehicles?](#) Automotive Daily. (2022, February 21).
- [7] Lu, S., Phung, B. T., & Zhang, D. (2018). [A comprehensive review on DC arc faults and their diagnosis methods in photovoltaic systems](#). *Renewable and Sustainable Energy Reviews*, 89, 88–98.
- [8] Xing, L., Wen, Y., Xiao, S., Zhang, D., & Zhang, J. (2022). [A deep learning approach for series DC arc fault diagnosing and real-time circuit behavior predicting](#). *IEEE Transactions on Electromagnetic Compatibility*, 64(2), 569–579.
- [9] Orendorff, C., Lamb, J., Nagasubramanian, G., Fenton, K., & Langendorf, J. (2015b, April). [Quantifying Thermal Runaway and Improvements Through Materials Development](#) (No. SAND2015-2970C). Sandia National Lab. (SNL-NM), Albuquerque, NM (United States).
- [10] Sheikh, M., Elmarakbi, M., Rehman, S., & Elmarakbi, A. (2021). [Internal Short Circuit Analysis of Cylindrical Lithium-Ion Cells Due to Structural Failure](#). *Journal of the Electrochemical Society*, 168(3), [030526].
- [11] [What Is Thermal Runaway? \(Fact Sheet\)](#). (2021, August 25). UL Research Institutes.
- [12] Schröder, R., Aydemir, M., & Seliger, G. (2017). [Comparatively Assessing different Shapes of Lithium-ion Battery Cells](#). *Procedia Manufacturing*, 8, 104–111.
- [13] Eberhard, M. (2010, September 15). [A Bit About Batteries](#). Tesla.
- [14] Nadimpalli, S. P., Sethuraman, V. A., Abraham, D. P., Bower, A. F., & Guduru, P. R. (2015). [Stress Evolution in Lithium-Ion Composite Electrodes during Electrochemical Cycling and Resulting Internal Pressures on the Cell Casing](#). *Journal of The Electrochemical Society*, 162(14), A2656–A2663.

- [15] Taheri, P., Mansouri, A., Yazdanpour, M., & Bahrami, M. (2014). [Theoretical Analysis of Potential and Current Distributions in Planar Electrodes of Lithium-ion Batteries](#). *Electrochimica Acta*, 133, 197–208.
- [16] Feng, X., Ouyang, M., Liu, X., Lu, L., Xia, Y., & He, X. (2018). [Thermal runaway mechanism of lithium-ion battery for electric vehicles: A review](#). *Energy Storage Materials*, 10, 246–267.
- [17] Huang, X. (2010). [Separator technologies for lithium-ion batteries](#). *Journal of Solid State Electrochemistry*, 15(4), 649–662.
- [18] Steele, L., Orendorff, C., Lamb, J., Spangler, S., Luketa, A., & Blanchat, T. (2015). [Understanding Lithium-Ion Battery Fires](#). Sandia National Laboratories. In Sandia National Laboratories (Ed.), *SAND2014-17294PE*.
- [19] Patil, D., McDonough, M. K., Miller, J. M., Fahimi, B., & Balsara, P. T. (2018). [Wireless Power Transfer for Vehicular Applications: Overview and challenges](#). *IEEE Transactions on Transportation Electrification*, 4(1), 3–37.

Abbreviations and Acronyms

ACRONYM	DEFINITION
ADC	Analog to Digital Converter
AI	Artificial Intelligence
AFCI	Arc Fault Circuit Interrupter
ARC	Accelerated Rate Calorimetry
EV	Electric Vehicle
FEA	Finite element analysis
FEDS	Fire an Explosion Detection System
FFT	Fast Fourier Transform
ICR	Manufacturer Acronym (LCO)
IFR	Manufacturer Acronym (LFP)
IMR	Manufacturer Acronym (LM)
INR	Manufacturer Acronym (NMC)
IPT	Inductive Power Transfer
IR	Infrared
ISC	Internal Short Circuit
LCO	Lithium Cobalt Oxide
LFP	Lithium FerroPhosphate
LIB	Lithium-ion Battery
LM	Lithium Manganese
LMO	Lithium Manganese Oxide
MCU	Microcontroller Unit
NCA	Nickel Cobalt Aluminum
NCO	Nickel Cobalt Oxide
NEC	National Electrical Codes
NMC	Nickel Manganese Cobalt
PPE	Personal Protective Equipment

ACRONYM	DEFINITION
Rx	Receiver
SOC	State of Charge
STFT	Short Time Fourier Transform
TC	Thermocouple
TR	Thermal Runaway
TRL	Technology Readiness Level
Tx	Transmitter
WT	Wavelet Transform
ZVS	Zero Voltage Switching